Journal of Radiation and Nuclear Applications
An International Journal

http://dx.doi.org/10.18576/jrna/080308

Mineralogical, Radiological and Geochemical studies on Wadi Sikait gneisses, South Eastern Desert, Egypt.

Ismail, A. M[*]

Nuclear Materials Authority, P.O. Box: 530, Maadi, Cairo, Egypt.

Received: 02 Jul 2023, Revised: 04 Jul 2023, Accepted: 24 Aug. 2023.
Published online: 1 Sep 2023.

Abstract: The studied area is located between latitudes 24o38′ 36 ″ to 24o 39’ 21 ″ N and longitudes 34o 47′ 03 ″ to 34o 48′ 06 ″ E, which contain psammitic gneiss, ophiolitic mélange, monzogranites, and lamprophyre dykes. The rocks are jointed, sheared, mylonitized, and hematized and showing silicification. Petrographically the gneisses are composed of quartz, plagiocalse, k-feldspar and biotite. Sericitization and chloritization are the main alteration processes. The studied gneisses are considered high uranium high thorium rocks and show evidences of uranium migration. The presence of M-W type tetrad effect in these rocks illustrate vigorous physic-chemical changes associating with gold mineralization. Fractionation of isovalents confirm these changes. The detailed mineralogical studies indicate the presence of mineral groups such as accessory minerals (zircon, apatite, aeschynite and columbite), the radioactive minerals (kasolite, torbernite, thorite, and uranothorite) and base metals (gold, bismite, cassiterite, chalcocite, and Sphalerite).

Keywords: gneisses, Sikait, paragneiss, Eastern desert.

1 Introduction

Wadi Sikait area is about 95 km southwest of Marsa Alam, in the south Eastern Desert (ED) of Egypt. The Nugrus – Sikait area covers about 320 km2 and constitutes a part of the Arabian Nubian Shield (Fig. 1) bordering the major shear zone known as Nugrus thrust fault [1], or Nugrus strike-slip fault [2] and Sha’it-Nugrus shear zone. [3] illustrated this shear zone as a boundary between Hafafit complex (high-temperature metamorphic rocks) in the SW and Ghadir group (mainly low-grade ophiolitic and arc volcanic assemblages). The Nugrus thrust runs along the upper part of W. Sikait in NW direction till the southern tip of G. Ras Sha’it, then swings to a southwestward direction along W. Sha’it west of G. Migif. W. Abu Rusheid lies in the west of W. Sikait and Sikait- Abu Rusheid pluton is elongated in NW-SE (12 km in length) and thinning in NE-SW (3 km in width).

In the northern part of the wadi, metamorphosed sandstone existed in two parts and has a high concentration of uranium and molybdenum. There are also gneiss rocks that occur in the middle part of W. Sikait, which contain radioactive minerals like thorite, uranothorite, and base metals. [4], [5],[6], [7].

The present study aims to throw light on the mineralogical and geochemical characteristics further to the radioactivity of the mineralized zone of wadi Skait psammitic gneiss at the contact of ophiolitic mélange, the monzogranites rocks and cutted by lamprophyre dykes.

2 Materials and Methods

A portable differential gamma-ray spectrometer model Rs-230 BGO Super-Spec, serial No. 4333, manufactured by Radiation Detection Systems AB, Backehagen 35, SE-79191 FALUN, Sweden was used to collect field radiometric survey measurements of eU (ppm), eTh (ppm), and K percent. the reading was given directly every 30 seconds.

8 samples of psammitic gneiss and 10 samples from anomaly spots were carefully selected for the geochemical and mineralogical investigations. The representative samples (each sample weight approximately 3 kg) were collected from the selected stations depending on the

[*]Corresponding author e-mail: a.m.ismail302@gmail.com

variation in composition and field radiometric measurements.

The collected samples were crushed, grinded, and quartered. The sample was sieved into three fractions: <800µm, 800µm-63µm, and> 63µm. The fraction size ranging between 800µm-63µm for each sample was subjected to heavy liquid separation using bromoform solution (sp. gr. 2.81 g/cm3) to separate the heavy minerals. Under the Binocular stereo-microscope, the acquired heavy mineral fractions were studied. The picked mineral grains were investigated by Environmental Scanning Electron Microscope (ESEM) (XL30-ESEM, Philips) attached with EDX microanalysis unit developments in 30 kv. (low-vacuum) and by X-ray diffraction (XRD) technique for mineral identification (device model: Malvern Panalytical Empyrean, (2020) (Netherlands). These analyses were carried out in the laboratories of the Nuclear Materials Authority (NMA), Cairo, Egypt. many samples were chosen, prepared as thin sections, and studied using the transmitted light polarizing microscope (Olympus-BZ70) equipped with Olympus digital camera.

A special process was required to determine the amount of gold in the sample. At EMRA, a fire assay analysis was performed. Fifty grams of sample (crushed and sieved to 200 Mesh) were burned in the presence of alkali fusion agents. The chemical concentrations of the major oxides, trace elements, and rare earth elements (REEs) were determined in Acme Lab, Vancouver, Canada by inductively coupled plasma emission spectrometry (ICP-ES). Detection limits for trace elements and major oxides were 0.01–0.5 ppm and 0.001 wt. %– 0.04 wt. %, respectively. The analytical accuracy, as calculated from replicate analyses, was 0.5% for major oxides and varied from 2% to 20% for trace elements.

3 Geologic Setting

The study area lies between latitudes 24°38′ 36 ″ to 24° 39′ 21 ″ N and longitudes 34° 47′ 03 ″ to 34° 48′ 06 ″ E (Fig. 2). The tectono-stratigraphic sequence begins from the oldest as follows; psammitic gneiss, ophiolitic mélange, monzogranites, and lamprophyre dykes [8].
psammitic gneiss striking NNE-SSW contacted elongate with the ophiolitic mélange from the eastern side and the monzogranites from the other western part. The rocks are jointed, sheared, mylonitized, and hematized. The rocks show silicification and banding with dipping 50°-69° to NNW-W directions (Fig. 3 a&b). The ophiolitic melange is concentrated in the eastern part of the mapped area and characterized by tectonically mixed fragments and blocks of ultramafic rocks within fine to coarse-grained matrix. There are sharp contacts with the mineralized zone of the gneisses in the western side of W. Sikait. It is composed mainly of melange matrix (mainly schists) that encloses abundant fragments of meta-peridotites, meta-pyroxenites, and metagabbros of variable sizes and dimensions [9]. Monzogranite rocks are concentrated in the western side of the mapped area. It is coarse to very coarse-grained, with K-feldspar crystals up to 2 cm in length, grey to white pinkish, and composed mainly of quartz, plagioclase, feldspars, and biotite. The rock is jointed, sheared, mylonitic, and hematitized in some parts. The porphyritic orthoclase perthite crystals form allotriomorphic plates showing preferred orientation parallel to the general direction of elongation of the biotite flakes.

The basic dykes in the study area are lamprophyre dykes. These dykes are almost vertical dip strikes NNW-SSE and intrudes the ophiolitic mélange, psammitic gneiss and monzogranites. It varies in thickness from 0.5 m to 1.5 m and extends more than one kilometer and is cut by right-lateral strike-slip faults.

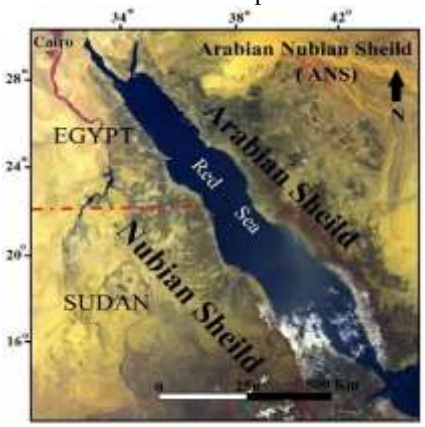

Fig. 1: The Arabian Nubian Shield (ANS), **[10]**. North Eastern Desert (NED), Central Eastern Desert (CED), and Southern Eastern Desert (SED).

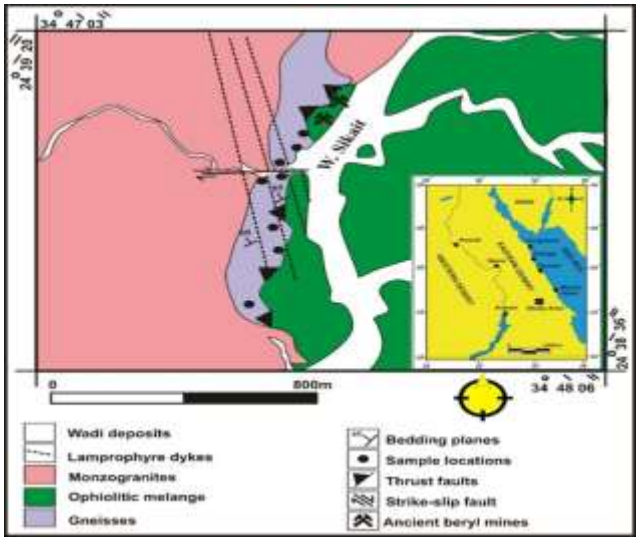

Fig.2: Geological map of W. Sikait, SED, Egypt [8].

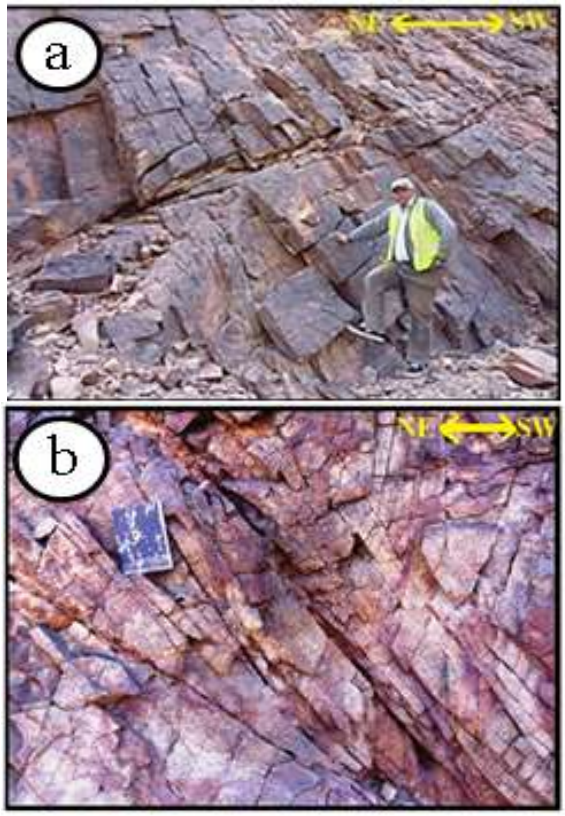

Fig. 3 a) banding in the gneisses with dipping 65° toward NW direction **[8]**. b) Shearing and hematitization of the psammitic gneiss.

4 Petrography

Psammitic gneiss is composed of quartz, plagioclase, biotite in addition to a less frequent amount of potash feldspar (microcline, microcline-perthite) (Fig. 4a). Zircon, monazite, cordierite, radioactive minerals, and opaques are common accessory phases.

The high-grade mineral assemblage is dominated by quartz (50 vol. %), plagioclase (30 vol. %), biotite (10 vol. %), K-feldspar, and cordierite are occasionally present.

Quartz is the most dominant mineral; it occurs in different forms reflecting variable degrees of dynamic metamorphism. The first stage is characterized by rounded to subrounded crystals, sometimes flattened with corroded boundaries preserving their wavy extinction (Fig. 4b).

The second stage is characterized by polygonal texture (tripple junction) where the equidimensional grains may have well-developed crystal faces resulting in straight grain boundaries, and where triple junctions are common (Fig. 4c).

The final intensive stage is characterized by the dominance of reworked quartz (fragmentation) and mortar texture formed during the event of dynamothermal metamorphism (Fig. 4d).

Plagioclase is dominated over alkali feldspar and exhibits wedged and flexure twins (Fig. 4e). Plagioclase appears as hypidiomorphic and xenomorphic crystals showing cloudy appearance characterized by medium grain size with lamellar twinning. It shows preferred directional orientation (Fig. 4f) and moderately affected by stress represented by breaking, bending and then dislocation of plagioclase (Fig. 4g). Some crystals of plagioclase have wedges of quartz crystals (Fig. 4h). It encloses minute crystals of zircon and monazite (Fig. 4 e&f).

K-feldspars are represented mainly by microcline and microcline perthite may occur as anhedral to subhedral crystals showing their characteristic cross-hatched and undulatory crosshatched twinning (Fig. 5a&b). Sericite represents the secondary phases where it is considered as an alteration product of K-feldspars (Fig. 5c).

Mica minerals are represented by biotite, phlogopite, and foliated flakes of muscovite. Biotite occurs as medium-sized flakes ranging from brown to greenish-brown in color; occasionally, it elongate parallel to the dominant foliation and alternating with the quartzofeldspathic components to produce the gneissose texture (Fig. 5d). In other samples, biotite is completely altered to chlorite and muscovite (Fig. 5e). Phlogopite occurs as stretched and deformed flakes with high interference colors (Fig. 5f). Muscovite is found as an alteration product of biotite "secondary muscovite" and is characterized by high interference color "fourth-order" (Fig. 5g).

Cordierite mostly is a product of metamorphism, booth contact and regional. Cordierite mineral occurs in a wide variety of regionally metamorphosed paraschists and gneisses and has developed over a wide range of pressure and temperature conditions.

Cordierite is present as hypidiomorphic crystals characterized by discontinuous twinning with wedged lamellae in the form of tip of a knife or pin which is characteristic in cordierite (Fig. 6a) or polysynthetic twinning (Fig. 6b).

Accessory minerals are mainly zircon, monazite, and radioactive mineral. Zircon occurs as tetragonal crystals that could be categorized into two types; the first shows as coarse crystals (1.2mm length) long-prismatic forms with obvious zoning (Fig. 6c). The second type is short-prismatic crystals exhibiting some features of radioactivity characterized by swollen and fractured boundaries (metamict zircon) (Fig. 6d). Sometimes zircon made denudation in mica (amoeboid fractured crystals) (Fig. 5f). Zircon is also present as euhedral crystal following the texture of gneissosity and perpenduclear on stress (Fig. 6e) or as distorted crystal (Fig.6f).

Monazite occurs as euhedral crystals included in plagioclase and microcline-perthite (Fig. 4f). Radioactive material was recorded as yellow amorphous material associated with iron oxides filling the late-stage fractures associating with iron oxides in the studied gneiss (Fig. 6g &h).

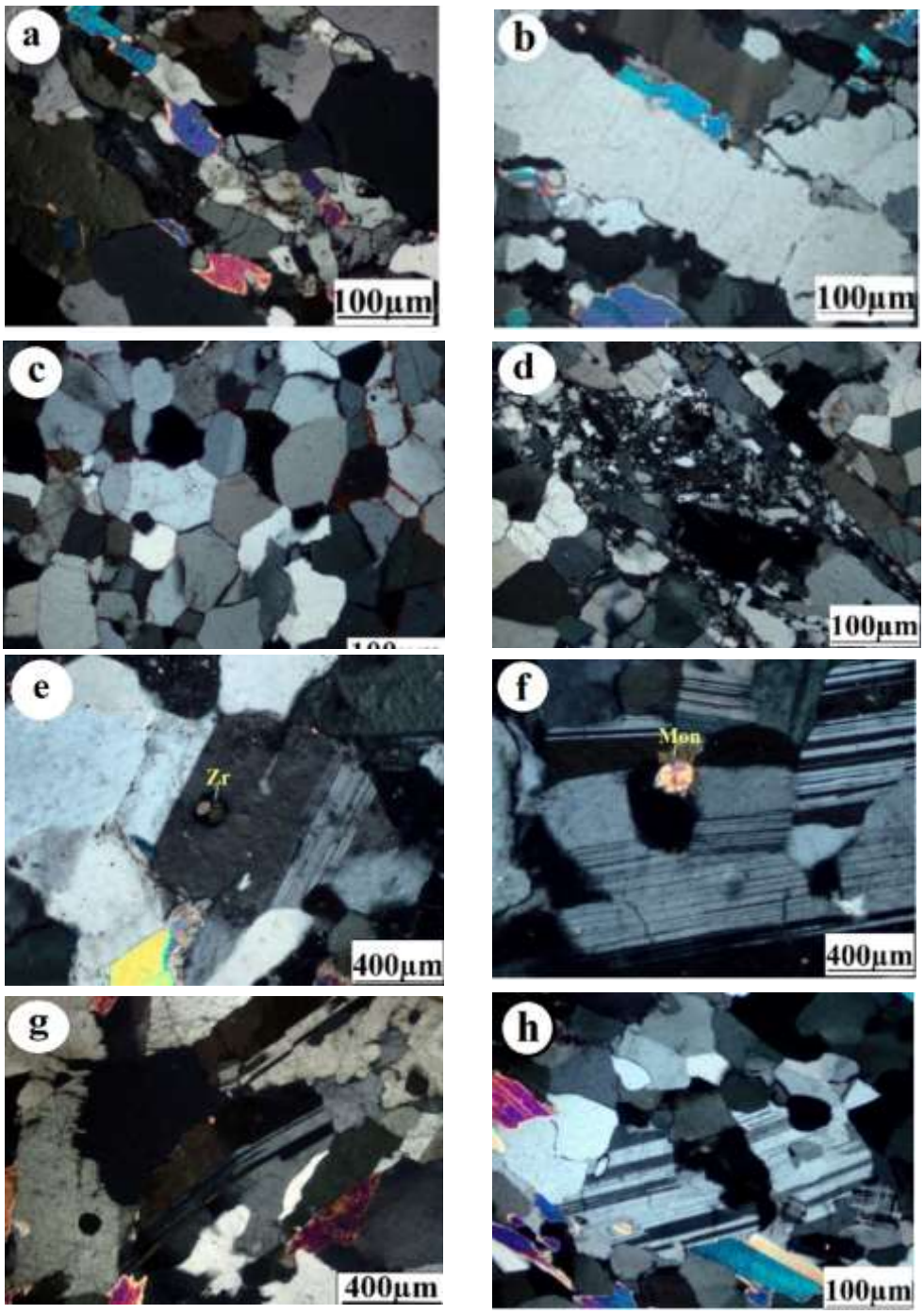

Fig. 4. Photomicrographs in Sikait psammitic gneiss showing: -
a) Bedding of quartz, feldspars and mafic, showing gneissosity, orientated gneissic foliation. CN.
b) Flattened Quartz crystals with corroded boundaries showing wavy extinction, CN.
c) Euhedral crystals of quartz showing tripple junction (Polygonal texture). CN.
d) Fragmented quartz forming mortar texture, CN.
e) Euhedral crystals of plagioclase encloses minute rounded crystals of Zr, CN.
f) Oriented crystals of plagioclase with Carlsbad twinning, CN.
g) Deformed crystal of plagioclase with dislocation, CN.
h) Plagioclase crystal corroded by wedges of quartz crystals, CN.

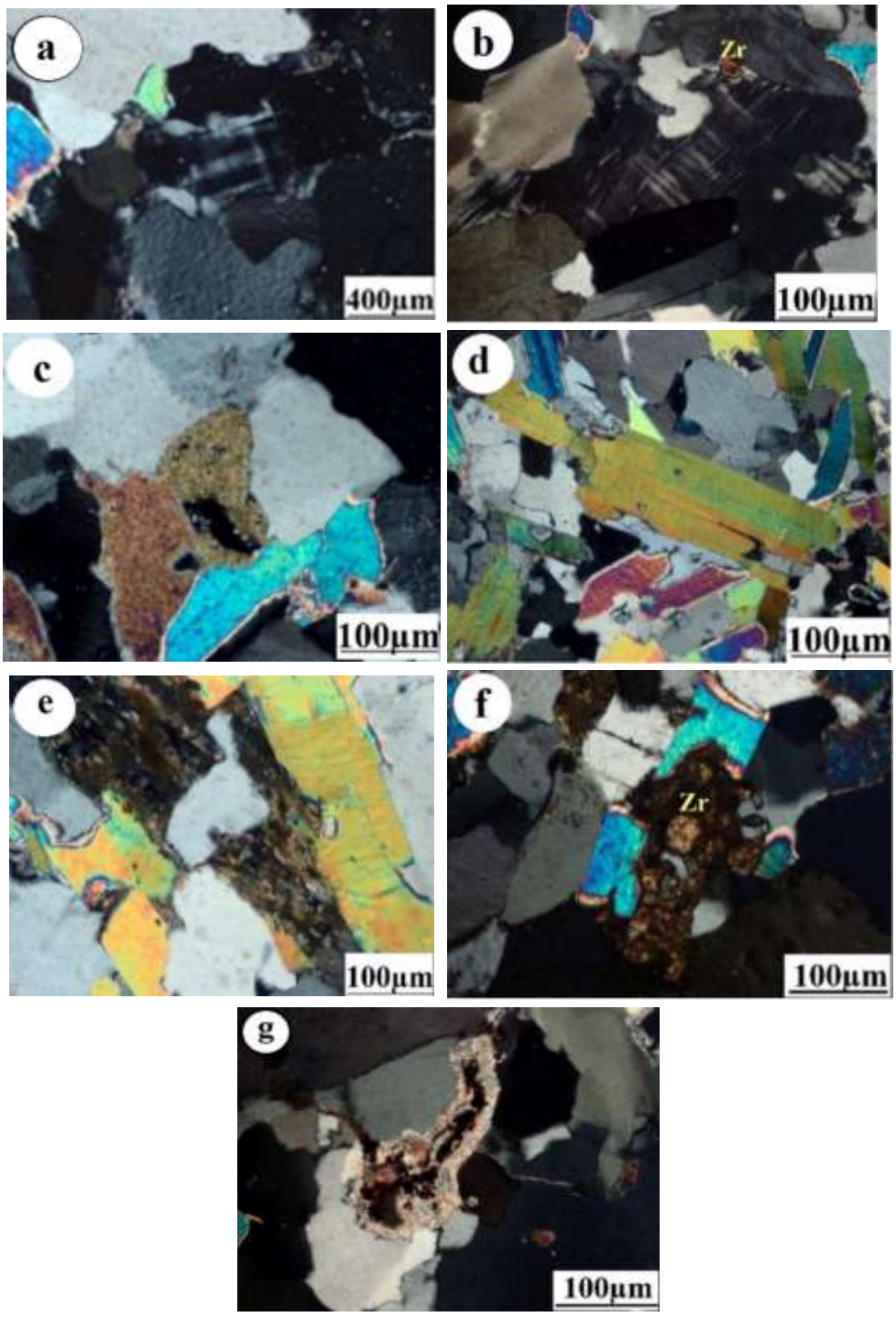

Fig. 5. Photomicrographs in Sikait psammitic gneiss showing: -

a) Subhedral crystal of microcline showing cross hatching, CN.
b) Unhedral crystal of microcline perthite, CN.
c) Subhedral crystal of sericite, CN.
d) Foliated flakes of biotite, CN.
e) Muscovitzation and chlorotization of BI, CN.
f) Denudation of mica (phlogopite) by zircon, CN.
g) Dissolution and replacement of quartz by secondary muscovite and Fe, CN.

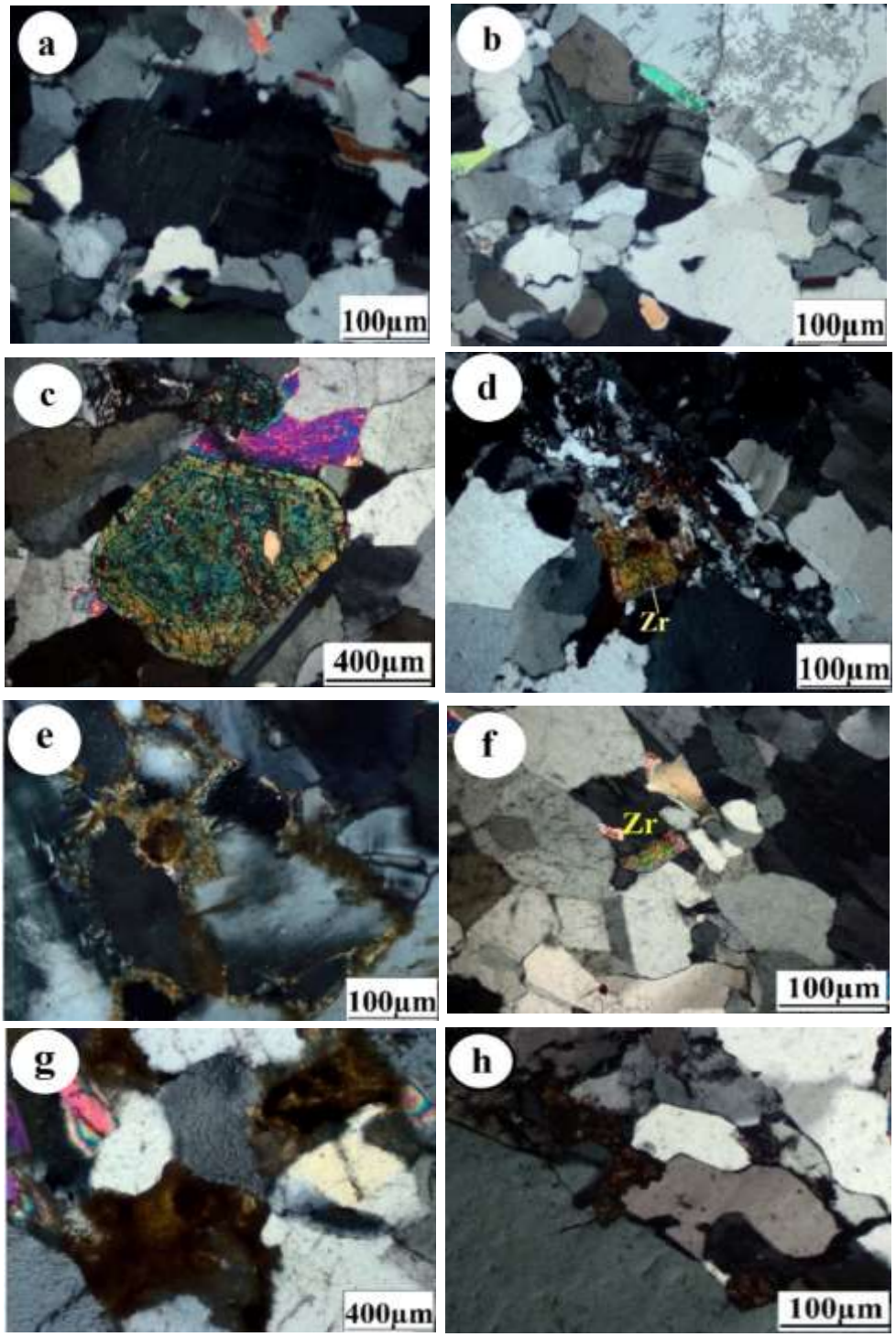

Fig. 6. Photomicrographs in Sikait psammitic gneiss showing: -
a) Discontinuous twinning with wedged lamellae in cordierite, CN.
b) Polysynthetic twinning in cordierite, CN.
c) Long-prismatic zircon with obvious zoning, CN.
d) Euhedral crystal of metamectized zircon crystal, CN.
e) Euhedral crystal of zircon following the texture of gneissosity and perpenduclear on stress, CN.
f) Distorted crystal of zircon, CN.
g) & (h) Opaque mineral surrounded by amorphous radioactive material, CN.

5 Mineralogy

5.1 Radioactive minerals

5.1.1 Kasolite [$Pb(UO_2)(SiO_3)(OH)_2$]

Kasolite is found as inclusion in quartz surface in gneisses and appear in pale yellow and greasy luster. The presence of kasolite was confirmed by X-ray diffraction (XRD), (Fig. 7a). The pattern shows the peaks at 2theta (30.61^o, 29.21^o, 25.15^o, and 27.10^o) with d-spacing (2.92, 3.06, 3.54, and 3.28 A^o) respectively match PDF-2 Card No. (29-788) of kasolite mineral. ESEM and semi-quantitative EDX analyses show that U concentration in kasolite (55-41 Wt. %) and Pb (35-36 Wt. %) (Fig. 7b).

5.1.2 Metatorbernite [$Cu(UO_2)_2(PO_4)_2$-$10H_2O$]

The metatorbernite mineral structure is mainly composed of phosphate tetrahedrons linked to U-O groups that form distorted octahedrons. The arrangement of phosphates and uranium groups are in sheets form that are bounded together by water molecules. The presence of metatorbernite was confirmed by X-ray diffraction (XRD), (Fig. 7c) The pattern shows the peaks at 2theta (15.22^o, 36.28^o, 38.36^o, and 26.90^o) with d-spacing (8.64, 3.67, 3.48, and 4.92 A^o) respectively match PDF-2 Card No. (86-1787) of metatorbernite mineral. the remnant peaks refer to associated quartz mineral. The EDX analyses indicate the chemical composition is U (65 Wt. %), P (8 Wt. %) and Cu (10 Wt. %) (Fig. 7d).

5.1.3 Thorite [$Th(SiO_4)$]

Thorite is a rare nesosilicate of thorium that crystallizes in the tetragonal system and is isomorphous with zircon and hafnium. It is the most common mineral of thorium and is nearly always strongly radioactive. The presence of thorite was confirmed by X-ray diffraction (XRD), (Fig. 8a). The pattern shows the peaks at 2theta (24.81^o, 18.92^o, 33.86^o, and 50.22^o) with d-spacing (3.58, 4.68, 2.65, and 1.82 A^o) respectively match PDF-2 Card No. (11-172) of thorite mineral. the other peaks refer to associated quartz mineral. The obtained ESEM data and its EDX reflect the chemical composition of the thorite Th (60 Wt. %), Si (13 wt. %) U (8 Wt. %), (Fig. 8b).

5.1.4 Uranothorite (U, Th) SiO_4

Uranothorite is considered as one of the radioactive minerals that are derived from the magma differentiation. Uranothorite may carry by the substitution for Th by U. The EDX analyses show that uranothorite has Th (70 Wt. %), and U (15 Wt. %) with traces of Y and Fe (Fig. 8c).

5.2 REEs minerals

5.2.1 Monazite (Ce, La, Th) PO_4

In the study area, monazite appear in reddish-brown color, opaque diaphaneity with vitreous luster. Monazite mineral identified by X-ray diffraction technique. its pattern (Fig. 9a) shows the peaks at 2theta (28.82^o, 31.22^o, 26.93^o, and 21.20^o) with d-spacing (3.09, 2.86, 3.31 and 4.19 A^o) respectively match PDF-2 Card No. (33-1095) of monazite mineral. EDX studies indicates various chemical compositions of monazite mineral, Th+ Si (25- to 38.5 Wt. %) and ∑REEs +P (45 to 74 Wt. %) (Figs. 9 b-c).

5.2.2 Rare Earth Silicate

In some cases, there are enrichments in Si at the expense of P. The EDX analyses show variation in the light rare earth silicate (LREE = 75 – 79 wt. %) (Fig.9 d).

5.3 Base metals

5.3.1 Gold (Au)

Gold (Au) is a transition metal between Ag and Rg in the chemical series of the Periodic Table. It found in the earth's crust 0.0035 ppm **[11]**. Gold occurs primarily as native minute inclusions and confirmed by fire assay analysis (0.82 g/t), ESEM analysis shows (Au 81- 50 Wt. %) (Fig. 10 a &b). It occurs coexist with Ag and Cu (~5-50 µm).

5.3.2 Bismite (Bi_2O_3)

It is the oxidation product of various bismuth minerals. Minute grains of native bismuth like ice crystal in shape were identified by EDX and reach 5 µm and have Bi (88.7 Wt. %) (Fig. 10 c & d).

5.3.3 Cassiterite (SnO_2)

Cassiterite is a tin oxide mineral with a chemical composition of SnO_2. It is the most important source of tin, and most of the world's supply of tin is obtained by mining cassiterite. The latter is more resistant to weathering than many other minerals. This mineral was recorded in gneiss as broad flakes (~20µm) and identified by X-ray diffraction technique. The XRD pattern (Fig. 10e) shows the peaks at 2theta (26.59^o, 33.89^o, 51.78^o, and 37.99^o) with d-spacing (3.35, 2.64, 1.76 and 2.36 A^o) respectively match PDF-2 Card No. (72-1147) of cassiterite mineral. the remnant peaks refer to zircon mineral PDF-2 card no. (1-679). EDX analysis indicate the percent of Sn (86 Wt. %) (Fig. 10 f).

5.3.4 Cuprite (Cu_2O)

It is an oxide mineral composed of copper oxide and is a minor ore of copper. Sometimes it called Ruby Copper and important ore of copper of secondary origin. Cuprite often occurs as well defined crystals embedded in oxidized portions of copper veins, and in masses in the midst of other copper ores, from which it was produced by oxidation processes. Cuprite suffers alteration very readily. It may be reduced to native copper, in which case the copper pseudomorphs the cuprite, or, on exposure to the air it may be changed into the carbonate, malachite, pseudomorphs of which after cuprite are common. The latter is recorded in paragneiss, having Cu 81Wt. % as confirmed by ESEM (Fig. 10 g).

5.3.5 Chalcocite (Cu_2S)

This mineral is also a secondary copper mineral founded in or near the oxidized zone of copper sulfide deposits. Regarding the forming chalcocite from pyrite, [12] believes that fluids contain copper sulfate can convert it to chalcocite according to the following reaction during a contact with pyrite and produce iron sulphate:

$$\mathbf{5FeS_2 + 14CuSO_4 + 12H_2O = 7Cu_2S + 5FeSO_4 + 12H_2SO_4}$$

It has been proved that chalcocite can be a suitable host for concentration of silver element [13]. Chalcocite was recorded in paragneiss and has irregular shape and shows a variable size with Cu (43 Wt. %) and S (32 Wt. %) (Fig. 10 h).

5.3.6 Chalcopyrite ($CuFeS_2$)

Chalcopyrite occurs as subhedral to euhedral crystals ranging in size from 50 to 200 m. chalcopyrite mineral identified by X-ray diffraction technique. The XRD pattern (Fig. 10 i) shows the peaks at 2theta (44.21°, 76.14°, 9.15 °, and 75.52°) with d-spacing (3.04, 1.85, 1.59 and 1.87 A°) respectively match PDF-2 Card No. (09-423) of chalcopyrite mineral.

The EDX analyses of the chalcopyrite reflect its chemical composition and gave Cu (35 Wt. %), Fe (21Wt. %), and S (26 Wt. %), together with minor Si and Ca (Fig. 10 j**).** This mineral has been often transformed into oxidized and carbonate phases as a result of oxidation. According to [14], chalcopyrite turns to malachite ($Cu_2(OH)_2CO_3$) on the effect of decomposition of diluting fluids with low copper concentrations and during the reaction with CO_2, as follows:

$$\mathbf{2CuFeS_2\ (Chalcopyrite) + 8.5O_2 + 2H_2O \rightarrow Fe_2O_3 + 2Cu^{2+} + 4SO_4^{-2} + 4H^+}$$

$$\mathbf{Cu^{2+} + H_2O \rightarrow CuO + 2H^+}$$

$$\mathbf{2CuO + CO_2 + H_2O \rightarrow Cu_2(OH)_2CO_3\ (Malachite)}$$

5.3.7 Chrysocolla

$(Cu, Al)_2H_2Si_2O_5(OH)_4 \bullet n(H_2O)$

It is typically found as rounded masses or crusts. the EDX analysis shows it contain Cu (54 Wt. %), Si (17 Wt. %), Al (8 Wt. %) with traces of Sn (10 Wt.%) (Fig. 10 k).

5.3.8 Sphalerite (ZnS)

Sphalerite is tetrahedral sulfides group minerals and is recognized by its luster, density and may be confined with galena but yield a brown streak. It is found in hydrothermal veins with pyrite and magnetite. In the study area, sphalerite mineral identified by X-ray diffraction technique. The XRD pattern (Fig. 10 l) shows the peaks at 2theta (33.27°, 55.68°, 66.41 °, and 76.84°) with d-spacing (3.12, 1.91, 1.63 and 2.74 A°) respectively match PDF-2 Card No. (77-2100) of sphalerite mineral.

the EDX analysis shows it contain Zn (57 Wt. %), S (31 Wt. %), with minor amounts of Fe (7 Wt. %) (Fig. 10m).

5.4 Nb- Ta Minerals

5.4.1 Ferrocolumbite (Fe, Mn) (Nb, Ta) O_4

Columbite is iron-black, grayish, and brownish black, opaque, rarely reddish brown and translucent. The columbite group of minerals comprises many structurally related orthorhombic AB_2O_6 compounds (B= Ta, Nb). ferrocolumbite mineral identified by X-ray diffraction technique. The XRD pattern (Fig. 11 a) shows the peaks at 2theta (30.07°, 24.22°, 35.95 °, and 25.19°) with d-spacing (2.97, 3.67, 3.49 and 2.53 A°) respectively match PDF-2 Card No. (79-1521) of ferrocolumbite mineral.
the EDX analysis shows it contain, Nb (54 Wt. %), Ta (4 Wt. %) and Fe (17 Wt. %) (Fig. 11b).

5.4.2 Aeschynite $(Y,Ca,Fe)(Ti,Nb)_2(O,OH)_6$

The obtained results indicate that the chemical composition of the studied aeschynite crystals is Ti (19 Wt.%), Nb (22 Wt. %), Y (15.6 Wt.%), Ta (2.2 Wt. %), U+Th (17 Wt.%), HREEs (8 Wt.%) and Fe (2 Wt. %) (Fig. 11 c)

5.5 Accessory minerals

5.5.1 Zircon ($ZrSiO_4$)

Zircon is fairly resistant to normal chemical attack [15]. The metamict state (breakdown of the structure) in zircon may be due, at least in part, to the presence of radioactive atoms. Recently, zircon is used as a guide for U mineralization [16], [17]. Zircon mineral identified by X-ray diffraction technique. The XRD

pattern (Fig. 12 a) shows the peaks at 2theta (26.75^{o}, 35.40^{o}, 19.78 ^{o,} and 53.13^{o}) with d-spacing (3.32, 2.53, 4.45 and 1.72 A^{o}) respectively match PDF-2 Card No. (81-588) of zircon mineral.

In the present study, the separated zircons are euhedral to subhedral prismatic and with thick width, some grains are rounded, and with zoned core and usually contain brownish- black radioactive inclusions and have relatively large sizes (Fig. 12 b&c), some crystals occur as solid solution with fergusonite (Fig.12d); others contain inclusion of Bi (Fig. 12e).

5.5.2 Xenotime (HREE, Y, PO_4)

Xenotime is a rare mineral which occurs, like monazite, as an accessory constituent in granite, gneiss and gmatite veins and crystalline metamorphic rocks. Xenotime mineral appear in reddish brown, translucent to opaque. The mineral identified by X-ray diffraction technique. The patterns (Fig. 12f) show the peaks at 2theta (25.79^{o}, 34.93^{o}, 51.60 ^{o}, and 19.53^{o}) with d-spacing (3.45, 2.56, 1.77, and 4.54 A^{o}) respectively match PDF-2 Card No. (11-254) of xenotime mineral. The peaks at 2theta (26.67^{o}, 20.87^{o}, 50.17^{o}) refer to quartz mineral. The EDX data shows that xenotime is composed of Y (52 -24 Wt.%), P (20-24 Wt.%) and HRREs (15.8-26 Wt.%) (Fig. 12 g).

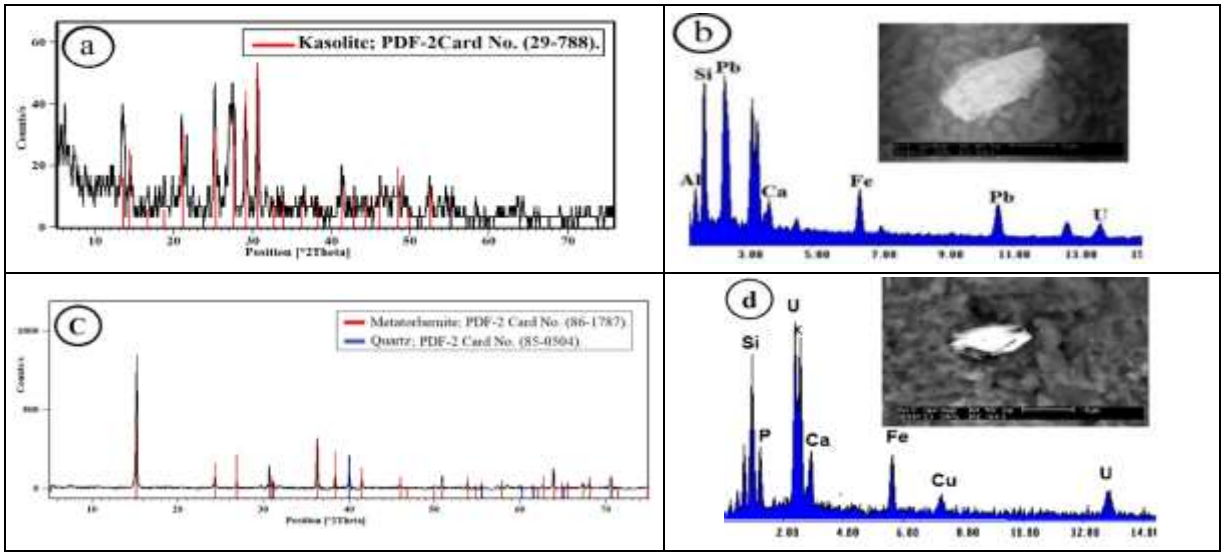

Fig. 7 showing XRD pattern, EDX and BSE images of (a,b) Kasolite, (c,b) metatorbernite uranium minerals.

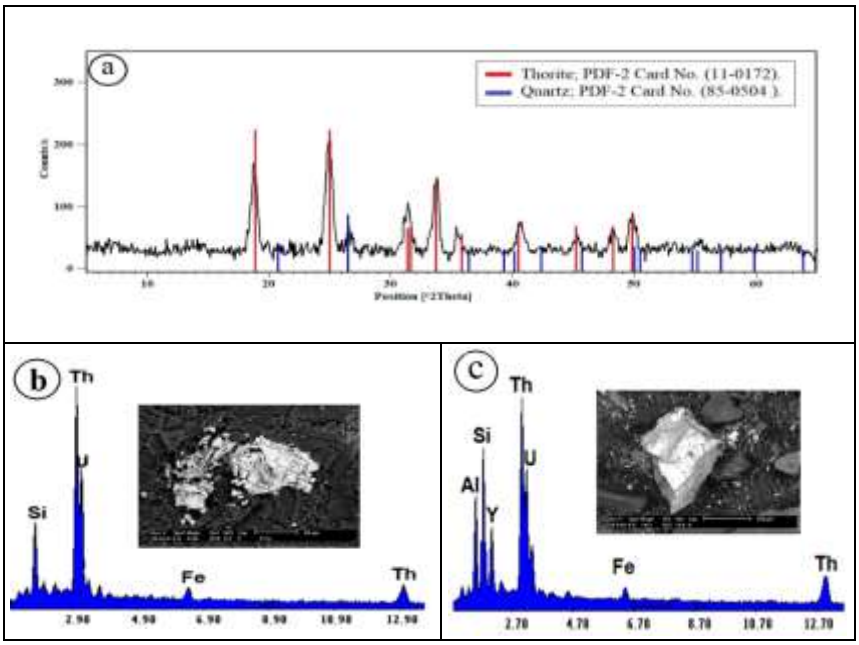

Fig. 8 showing (a,b) XRD pattern, EDX and BSE images of thorite mineral, c) EDX and BSE of uranothorite mineral.

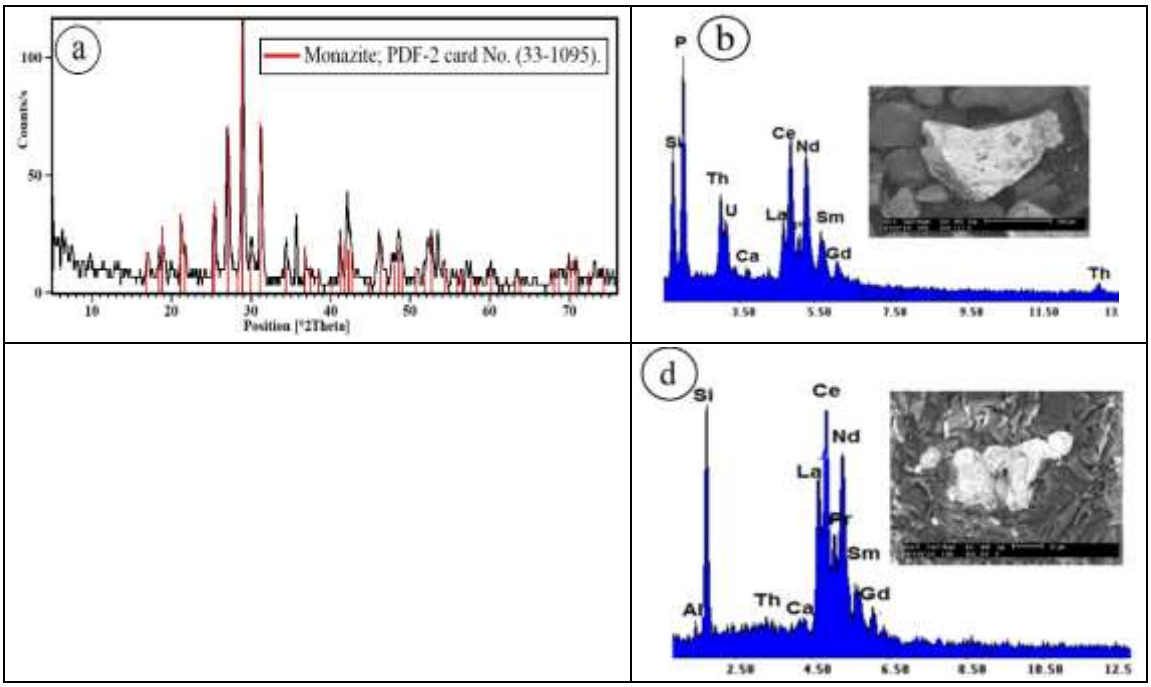

Fig. 9 showing (a,b,c) XRD pattern, EDX and BSE images of monazite mineral. d) REEs minerals.

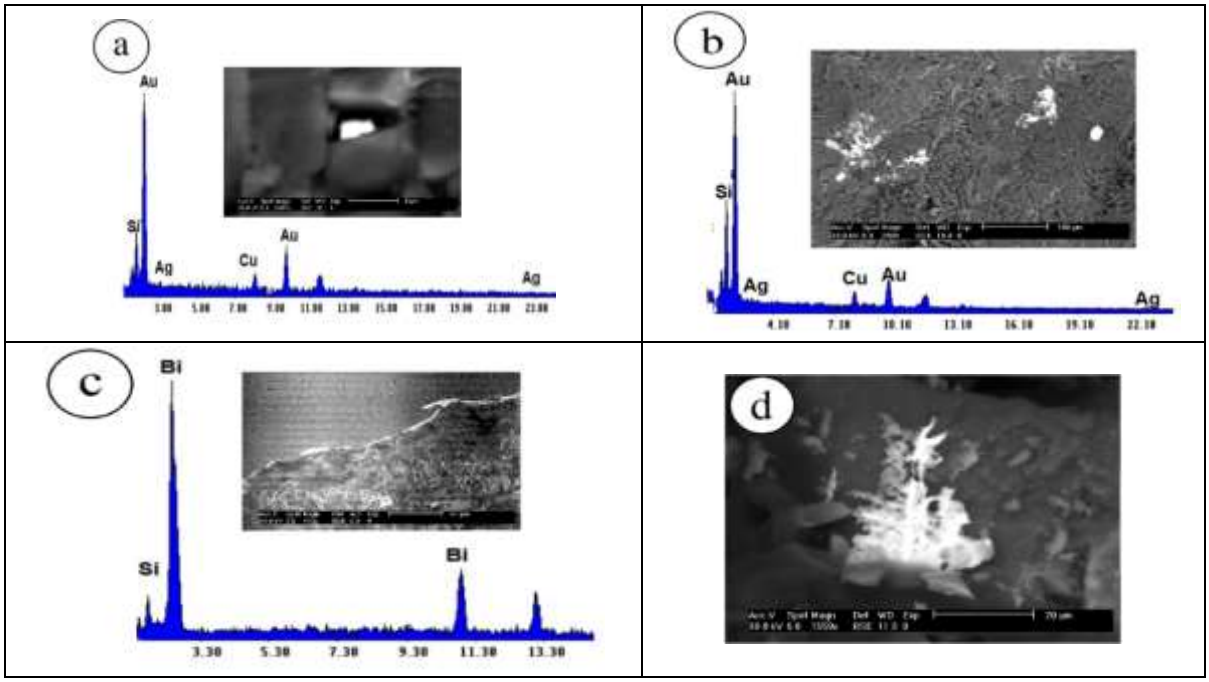

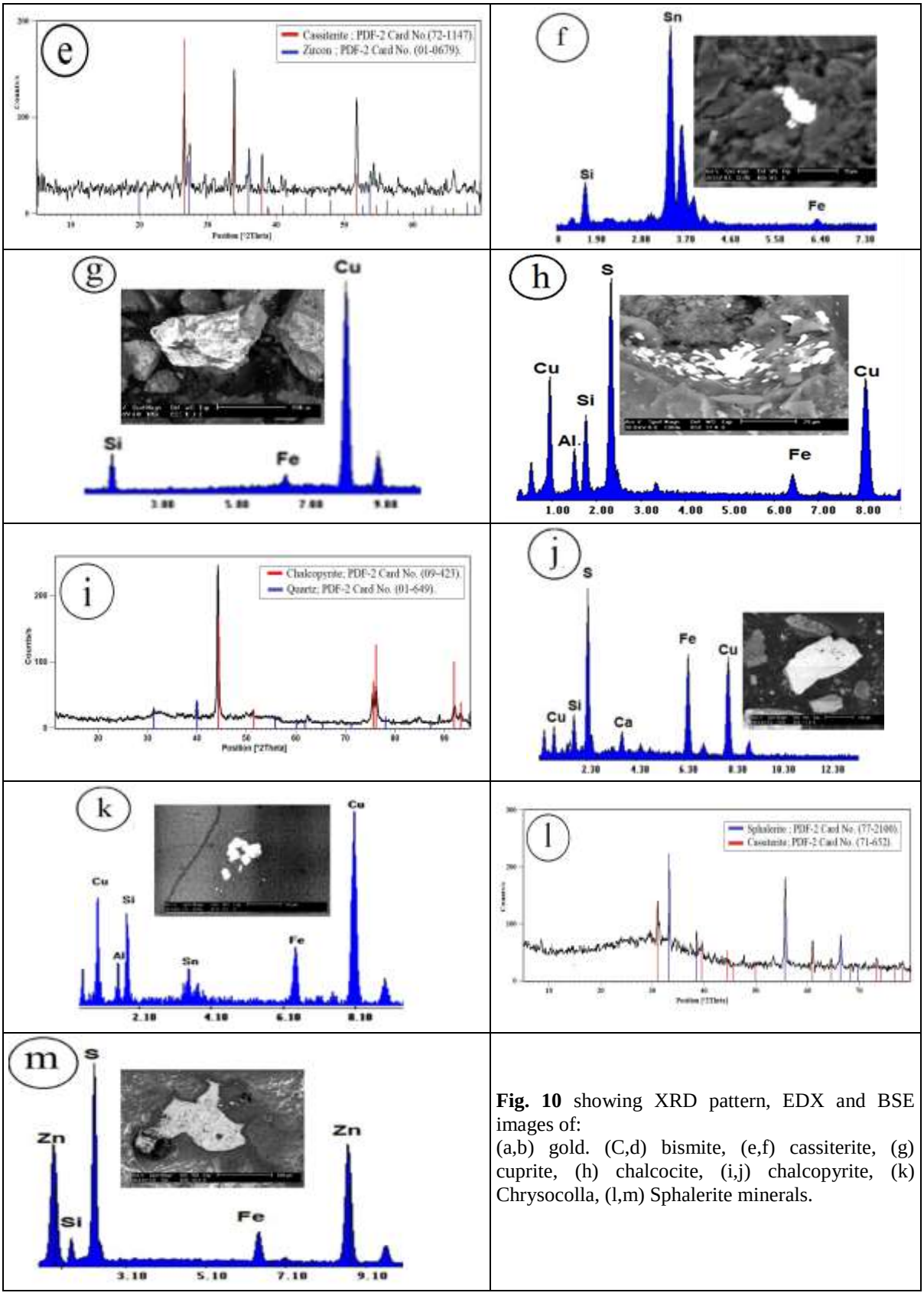

Fig. 10 showing XRD pattern, EDX and BSE images of:
(a,b) gold. (C,d) bismite, (e,f) cassiterite, (g) cuprite, (h) chalcocite, (i,j) chalcopyrite, (k) Chrysocolla, (l,m) Sphalerite minerals.

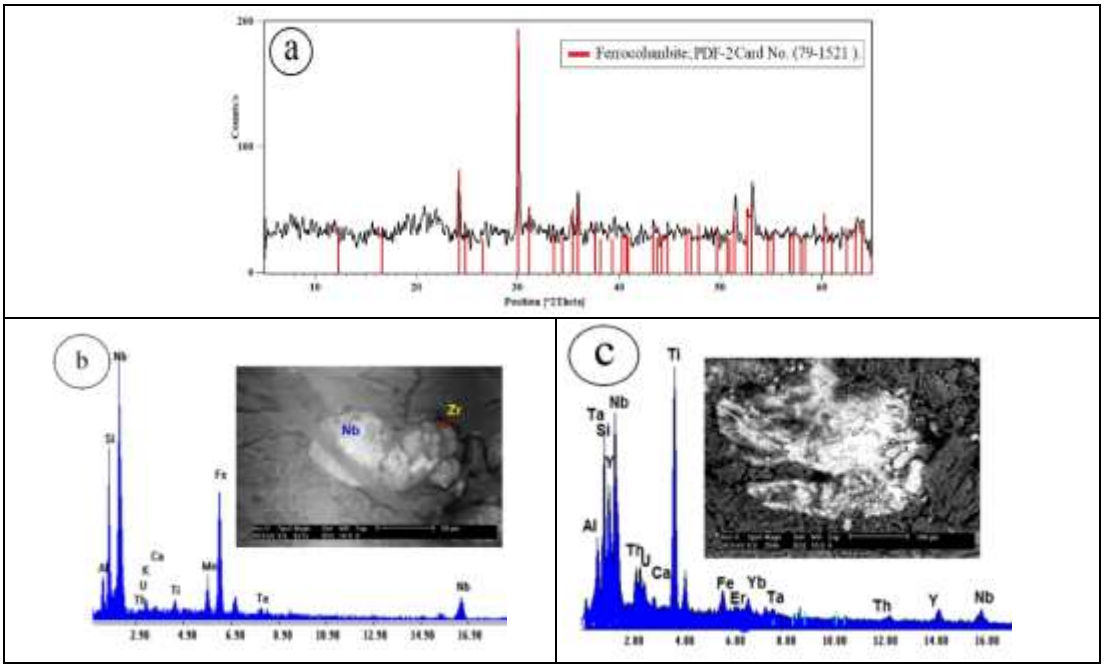

Fig. 11 showing XRD pattern, EDX and BSE images of (a,b) ferrocolumbite mineral (c) EDX and BSE images of aeschynite mineral.

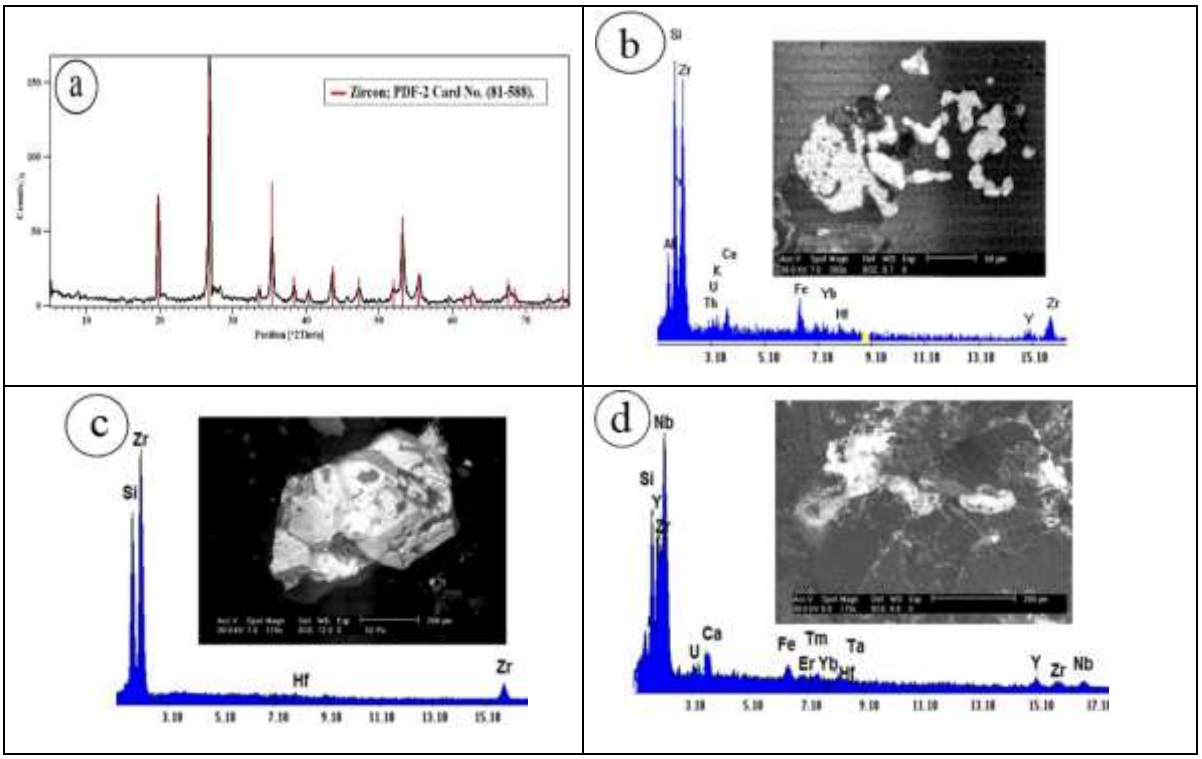

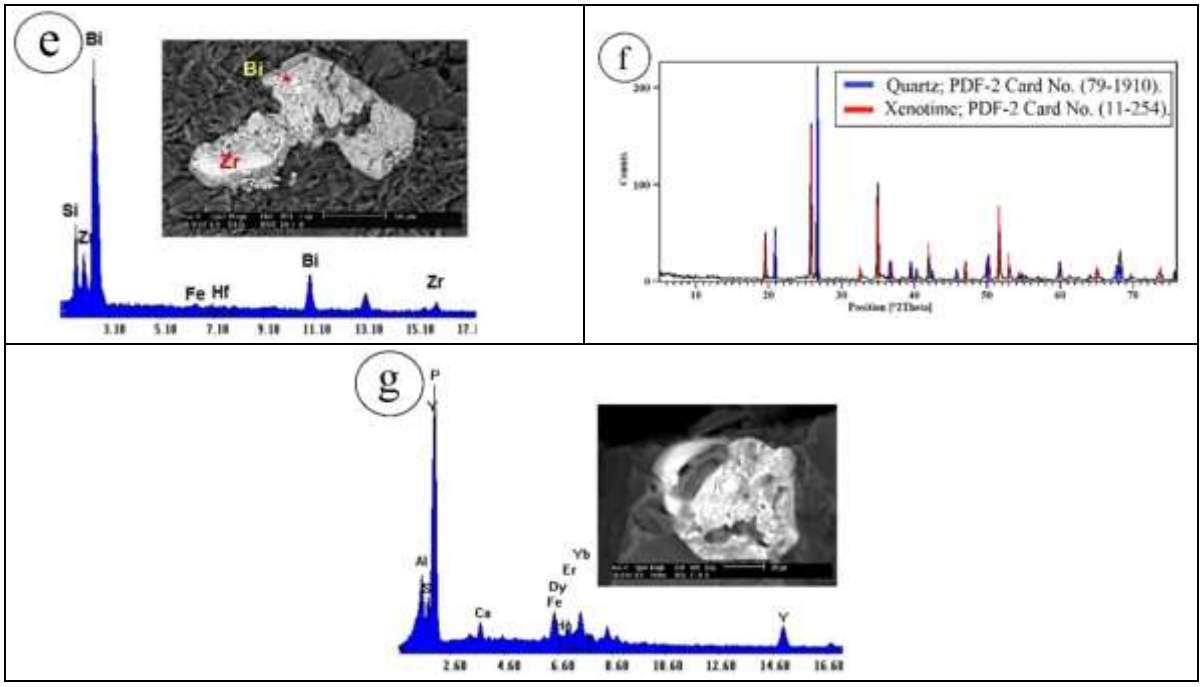

Fig. 12 XRD pattern of Back scattered images and EDX data of (a-e) zircon, (f&g) xenotime minerals.

6 Geochemistry

Eight representative samples of psammitic gneiss from Wadi Sikait were analyzed for their whole-rock major, trace and rare earth elements contents. The samples were analyzed by ICP-MS in the laboratory of Canada-Acme (Table 1,2). The analytical data have been plotted on diagrams to reveal the primary features of the protoliths. Geochemical data clearly reveal compositional variations of the primary sedimentary rocks.

Ten samples were measured and analyzed radiometrically in the laboratory of Nuclear Materials Authority by NaI (Tl) detector (Table 3).

The bulk-rock major and trace element geochemistry provide, in some cases, major constraints on both the nature and the provenance of the putative protoliths for high-grade metamorphic rocks e.g. [18], [19], [20], [21], [22], [23].

The samples from the Sikait psammitic gneiss show a relatively wide compositional range with SiO_2 between 73.2 and 76.3 % and Al_2O_3 between 10.6 and 14.9%. This is illustrated by a P_2O_5/TiO_2 versus MgO/CaO discrimination diagram [24], which, because the samples mostly tend to cluster above the discriminant line separating igneous from sedimentary rocks, establishes that they were of sedimentary origin (Fig. 13). However, on this diagram it must be remembered that the discriminant line is interpreted as a maximum value for igneous rocks: sedimentary rocks directly derived with little weathering from an igneous protolith can also plot below the line in the igneous field. On this basis, therefore the Sikait metamorphic association should be regarded as paragneisses. The empirical discrimination ratio 100TiO2/Zr (wt.% /ppm) based on transition metals (Ti) and HFSE (Zr), which are assumed to have an immobile behavior during metamorphism, is lower than 0.4 in all the analyzed paragneisses (Av. 0.015) and points to a significant input of psammatic material to the original clastic sequence [25], [23].

In the log Fe_2O_3/K_2O vs. log SiO2/Al2O3 classification diagram of [26], the investigated gneisses plot straddle between the lith-aranite, arkose and wake domains (Fig. 14). Also, discrimination of the protoliths after [27] pointing to greywake domain (Fig. 15). Th/Sc versus Zr/Sc diagram [28] indicated that the samples tend to have sedimentary recycling (Fig. 16).

6.1 Rock alteration

AKF diagram after [34] reveals that the most of studied psammitic gneiss samples have sercitie composition (Fig. 17). (MgO+Fe2O3) versus (Na2O+CaO) Diagram (Fig. 18) [35] pointed to the studied gneisses plotting in srectitization plagioclase destruction.

The degree of source area weathering recorded can be determined by the chemical index of alteration, CIA [36]. This index can be calculated by: CIA = $\{Al_2O_3/(Al_2O_3+CaO^*+Na_2O+K_2O)\}$ x 100. CIA values for the studied gneisses samples have an average 61.8% (Fig. 19). indicative of low to moderate degrees of chemical weathering for the parent rocks. However, it has been argued that CIA may not directly reflect the paleoweathering conditions especially in sediments with

variable provenances. Plotting CIA into A (Al_2O_3) – CN (CaO^*+Na_2O) - K (K_2O) compositional diagram can effectively evaluate chemical weathering, diagenesis metamorphism and source composition of clastic sediments [37], [38], [39], [40].

The CIA values are higher than average value of avarege upper contintal crust UCC [41] (50%) and fresh granite (47%). The higher CIA values suggest intense weathering of the first cycle sediment or recycling in humid and warm paleoclimatic conditions.

Weathering effects also can be evaluated in terms of the molecular percentage of the oxide components, using the formulae: chemical index of weathering (CIW) = $Al_2O_3/(Al_2O_3 + CaO^* + Na_2O)$ based on [42]. The CIA and CIW are interpreted in similar way with values of 50 for unweathered upper continental crust and roughly 100 for highly weathered materials, with complete removal of alkali and alkaline-earth elements [43], [28], [44]. Low CIA values (i.e. 50 or less) also might reflect cool and / or arid conditions [37]. The intensity of the chemical weathering can also be estimated using the Plagioclase Index of Alteration [31] in molecular proportions: PIA = $[(Al_2O3-K_2O)/ (Al_2O_3 + CaO^* + Na_2O-K_2O)] \times 100$.

Unweather plagioclase has PIA value of 50. The PIA values for the Sikait gneisses have an average 65.9%, also indicating moderate degree of weathering. The Mineralogical Index of Alteration (MIA) proposed by [45] is another weathering parameter calculated as: MIA = 2*(CIA- 50). MIA values between 0 and 20% are designated as incipient, i.e. just starting; 20-40% (weak); 40-60% (moderate) and 60-100% as intense to extreme degree of weathering. MIA value (Average = 24.33%), which indicates weak weathering condition.

Average CIA, PIA and CIW values of the samples indicate moderate weathering in the source area. According to ICV values and major and certain trace elements of gneisses rocks suggest that these samples are derived from the felsic rocks.

Some major element contents of rocks provide useful information on climatic conditions in the source area. On the binary SiO_2 versus ($Al_2O_3 + K_2O + Na_2O$) diagram [46] studied samples plot in the semiarid climate field (Fig. 20). Moreover, in the ICV-CIA diagram (Fig. 21), the samples are plotted in line between immature and mature, weak weathering areas, which suggest that the recycling did not have a strong effect on the CIA values, and the CIA values can reflect the paleoweathering conditions.

hydrothermal and diagenetic alteration box plot diagram (Fig. 22&23) for Sikait gneisses samples, after [47], The alteration box plot is a graphical representation that uses two alteration indices: the Ishikawa alteration index (AI) = 100 (K_2O+ MgO)/ (K_2O + MgO + Na_2O + CaO) and the chlorite carbonate pyrite index (CCPI) = 100 (MgO + FeO) / (Mgo + FeO + Na_2O + K_2O. The samples ploted in the least altered box in the field of K-feldspar-ab and Ab-Chl.

6.2 REEs geochemistry

Seven samples of psammitic gneiss were analyzed for REEs using the ICP-MS method (Table 2). Geochemistry of Rare earth elements (REEs) for the investigated psammitic gneiss reveal that the overall REEs ranges between 11 and 139 ppm for the psammitic gneiss.

Figure 24 illustrates the REE chondrite normalized patterns for representative samples of the paragneiss. Overall, these patterns are characterized by moderate LREE / HREE , flat HREE profiles and negative Eu anomalies of small amplitude (Eu/Eu* = 0.2). These negative anomalies signify considerable metasomatism and fractionation.

Rare earth element values are used as indicators of sedimentary provenance. Since they do not undergo the fractionation in granulite facies metamorphism, they yield reliable data for the interpretation of source rocks [48]; [49]. In chondrite-normalized REE diagrams, Eu anomalies are chiefly controlled by feldspar content of the rocks, because Eu is compatible in plagioclase and potassium feldspar. Negative Eu anomalies are present in all samples. The REE chondrite-normalized patterns and europium anomaly of clastic sedimentary rocks are also used to provide important clues regarding the source rock composition [41], [50].

Mafic rocks show less fractionated chondrite-normalized patterns with low LREE/HREE ratios and no or small Eu anomalies, whereas felsic rocks usually show fractionated chondrite normalized patterns with high LREE/HREE and negative Eu anomalies [51], [52], [41] as in Wadi Sikait psammitic gneiss (Table 2).

The perceptible negative Eu anomaly is either due to the partitioning of Eu into feldspar during fractionation, which is an important process in developing peralkalinity, or the presence of residual feldspar in the source [53].

Another alternative explanation for the negative Eu anomaly is based on the high oxygen fugacity in the melt due to volatile saturation [54].

Ce/Ce* in all samples are positive Ce anomaly, suggests the oxidizing condition, under which the REEs were precipitated, where cerium oxidizes to its immobile Ce^{4+} state.

$Ce/Ce^*=Ce_N/ (La_N\times Pr_N)^{0.5}$

$Eu/Eu^*=Eu_N/(Sm_N\times Gd_N)^{0.5}$

CC1, CC2 and CC3 ratios of the corresponding ∑REE contents of a paragneiss variety to their total Clarke contents ($\sum REE_{Cl}$ = 189.8 ppm, $\sum LREE_{Cl}$ = 158.4 ppm; $\sum HREE_{Cl}$ = 31.4 ppm, after [55].

Generally, there is enrichment in HREES in the most samples as compared with Clark values (Table 2).

Table 1 Chemical analysis of major oxides (wt.%), some trace elements (ppm) for Wadi Sikait psammitic gneiss.

	1	2	3	4	5	6	7	8	Avg.
SiO_2	74.5	75.2	74	75	75.2	73.2	76.3	74.82	74.78
TiO_2	0.073	0.07	0.063	0.116	0.033	0.088	0.086	0.08	0.08
Al_2O_3	11.52	11.71	10.64	12.22	14.89	12.66	11.69	12.3	12.20
Fe_2O_3	5.24	4.89	4.64	2.52	2.87	4.12	2.08	3.52	3.74
MnO	0.01	0.022	0.005	0.02	0.01	0.016	0.017	0.02	0.02
MgO	0.15	0.12	0.07	0.13	0.03	0.13	0.12	0.1	0.11
CaO	0.15	0.43	0.17	0.46	0.07	0.42	0.42	0.33	0.31
Na_2O	5.4	4.4	4.2	4	3.3	4.6	4.7	4.2	4.35
K_2O	1.2	2.1	4.1	4.3	1.2	3.6	2.6	2.98	2.76
P_2O_5	0.009	0.009	0.011	0.023	0.002	0.021	0.021	0.01	0.01
L.O.I	0.9	0.87	1.2	1.01	0.9	1	0.99	1	0.98
Total	99.15	99.82	99.1	99.8	98.51	99.86	99.02	99.35	99.33
S	0.04	0.07	0.04	0.04	0.08	0.28	0.23	0.12	0.11
CIA	63.05	62.82	55.68	58.25	76.52	59.49	60.23	62.17	62.28
PIA	65.03	66.55	59.95	63.97	80.25	64.35	63.97	66.51	66.32
ICV	1.06	1.03	1.25	0.94	0.5	1.02	0.86	0.93	0.95
CIW	67.5	70.8	70.9	73.3	81.5	71.6	69.5	72.93	72.25
MIA	26.1	25.64	11.36	16.5	53.04	18.98	20.46	24.33	24.55
Ba	60	70	75	190	28	70	72	84.2	81.2
Rb	103	161	290	250	167	164	160	198.7	186.7
Sr	28	36	26	52	10	36	35	32.5	31.9
Y	196	155	206	182	184	177	182	181	182.9
Zr	600	554	551	600	736	608	670	619.8	617.4
Nb	150	152	129	180	140	162	120	147.2	147.5
Th	20	31	30	24	40	25	20	28.3	27.3
Pb	10	13.8	12	20.3	15	8.5	9	13.1	12.7
Ga	36	41	40	30	26	42	44	37.2	37.0
Zn	43	50	101	54	86	42	43	62.7	60.2
Cu	53	11.5	50	20	140	85	80	64.4	63.0
Ni	3	1.3	1.3	3	2	3.2	3	2.3	2.4
V	4	3	2	4	2	4	5	3.3	3.4
Cr	82	50	30	23	77	56	53	48.2	52.4
Hf	4.3	7.4	3.1	3	1.2	4.4	3.3	3.7	3.8
Cs	1.2	1.2	1	2	2.3	1.2	1.3	1.5	1.5
Sc	1	0.8	0.6	1.2	0.5	1	0.8	0.8	0.8
Ta	10	13	11.5	7	1.1	11	11	9.1	9.2
Co	0.6	0.7	0.6	1.5	1	5	4.2	2.2	2.0
Li	31	50	20	56	38	39	41	40.7	39.5
Bi	8	6	6	0.5	15	9	10	7.8	7.8
U	15	13	16	7	20	8.8	8.7	12.3	12.6
W	8	9	11.5	10	6	12.5	13	10.3	10.0
Sn	40	82	25	30	67	40	40	47.3	46.4
Mo	2	1.7	1.08	4.4	2.2	1.4	1.5	2	2.0
Cd	0.1	0.1	0.12	0.02	0.5	0.44	0.4	0.3	0.2
As	2	0.2	0.2	0.2	0.5	0.5	0.2	0.3	0.5
Sb	0.08	0.06	0.02	0.14	0.1	0.04	0.04	0.1	0.1
Ag(ppb)	20	20	20	20	60	20	20	26.7	25.8
Zr/Hf	**139.53**	**74.86**	**177.74**	**200.00**	**613.33**	**138.18**	**203.03**	**167.51**	**162.47**
Nb/Ta	15.00	11.69	11.22	25.71	127.27	14.73	10.91	16.18	16.03

ICV = (Fe_2O_3+K_2O+Na_2O+CaO+MgO+MnO+TiO_2)/Al_2O_3 [29].
CIA = (Al_2O_3/(Al_2O_3+CaO*+Na_2O+K_2O) x 100 [30].
PIA = 100 × (Al_2O_3-K_2O) / (Al_2O_3+CaO*+Na_2O-K_2O) [31].

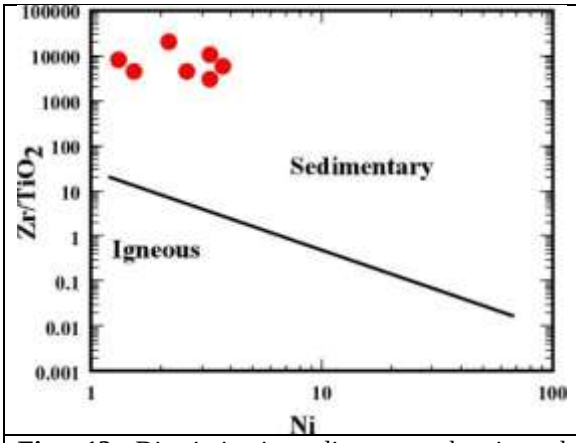

Fig. 13 Discrimination diagrams showing the chemistry of the sedimentary rocks from which the Sikait psammitic gneiss are derived: Zr/TiO2-Ni plot after **[32]** distinguishing igneous from sedimentary fields.

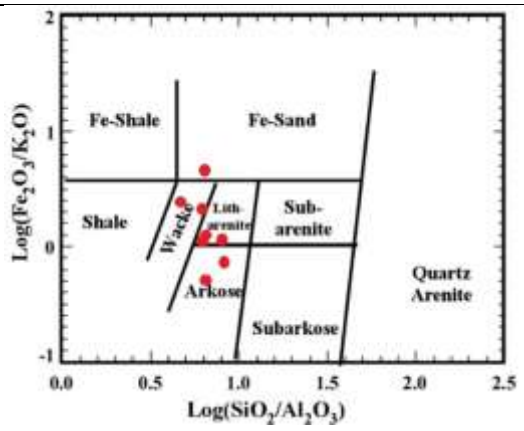

Fig. 14 Log (SiO_2/Al_2O_3) versus log (Fe_2O_3/K_2O) classification diagram of **[26]**.

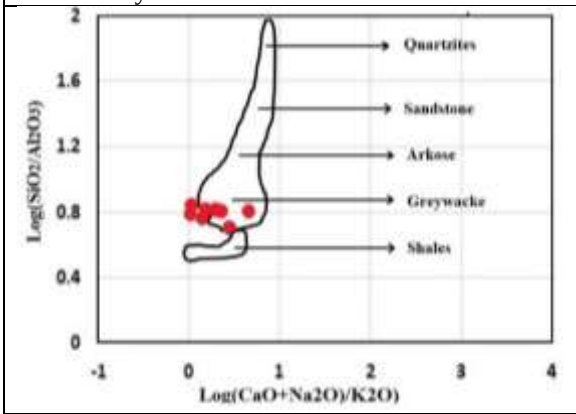

Fig. 15 Discrimination of the protoliths after **[33]**

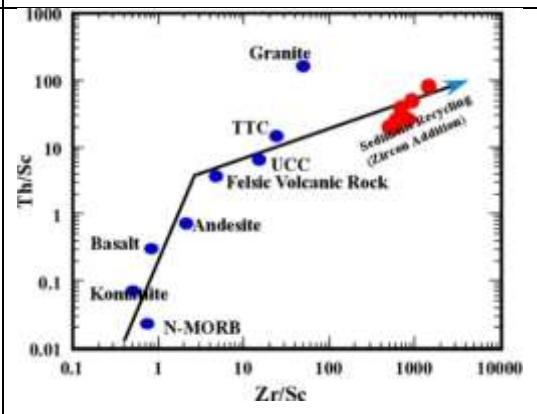

Fig. 16 Th/Sc versus Zr/Sc diagram **[28]** for the studied samples.

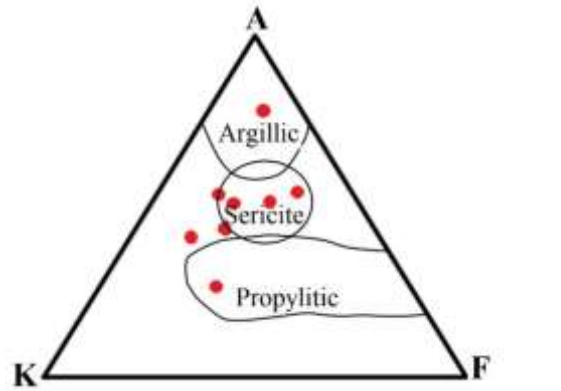

Fig. 17 AKF ternary diagram, after **[34]** A= Al_2O_3 – (Na_2O + K_2O), K= K_2O and F= FeO + MnO + MgO,

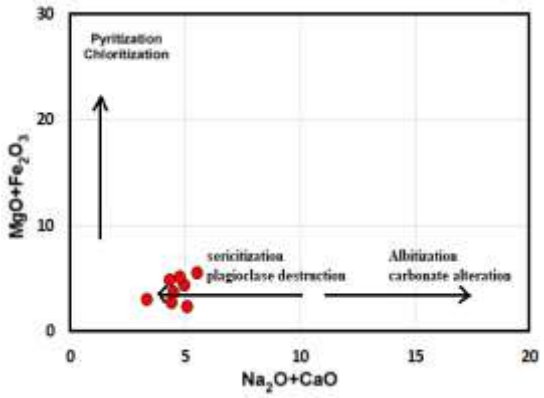

Fig. 18 (MgO+Fe2O3)-Na2O+CaO) Diagram after **[35].**

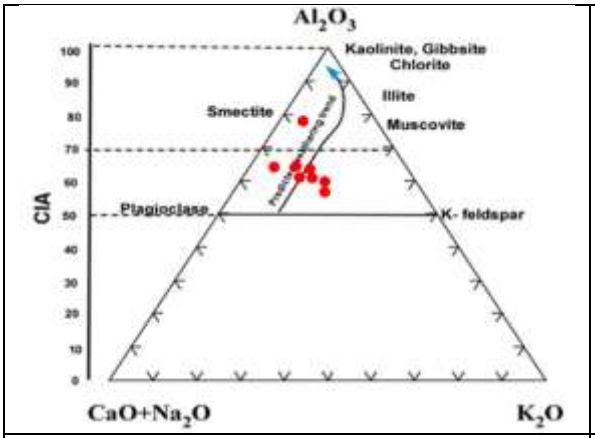

Fig. 19 Al2O3 – (Na2O + K2O) – K2O ternary diagram, showing the weathering trend, after **[40]**.

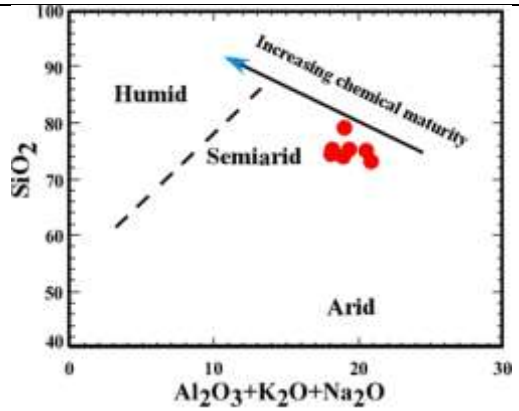

Fig. 20 Bivariate SiO_2 versus (Al_2O_3 + K_2O + Na_2O) paleoclimate discrimination diagram. Fields after **[46]**

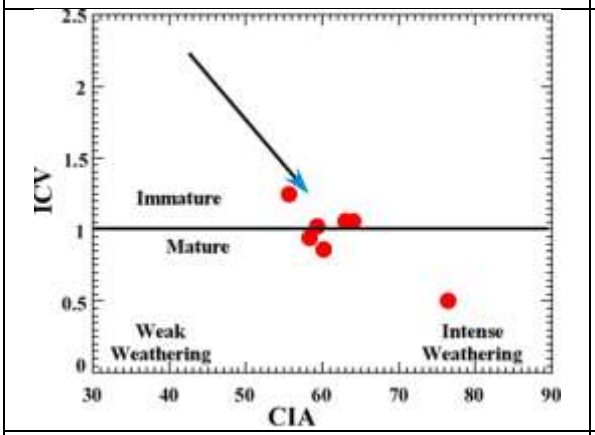

Fig. 21 CIA-ICV diagram after **[38], [29]**.

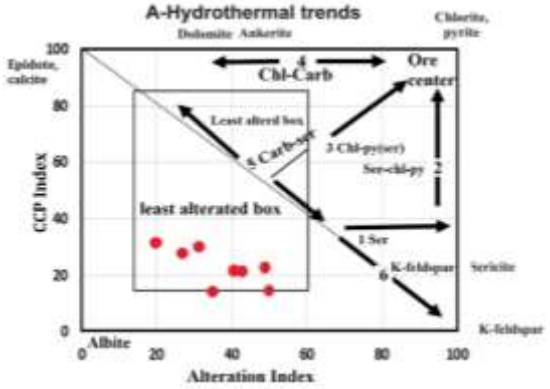

Fig. 22 hydrothermal alteration box plot diagram for Sikait gneisses samples, after **[47]**.

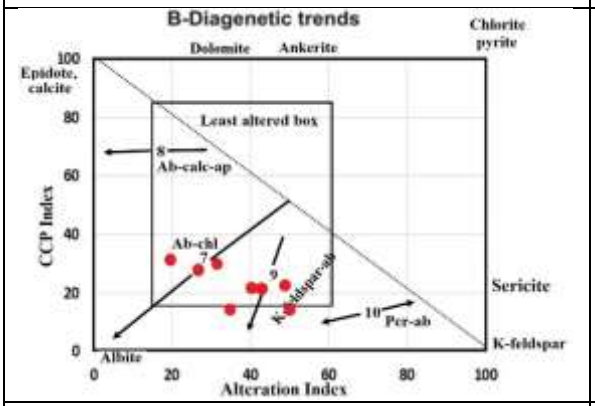

Fig. 23 diagenetic alteration box plot diagram for Sikait gneisses samples, after **[47]**.

Table 2 Rare Earth elements of Wadi Sikait psammitic gneiss.

sample	1B	2B	3B	4B	5B	6B	7B	Av.
La	2	6	13	21	1.1	6	6	8
Ce	5	10	40	50	4	20	17	21
Pr	0.7	1	5.2	6.5	0.5	2.5	2.3	3
Nd	2.1	2.4	16	23	14	8.2	8	11
Sm	1	1.2	5.4	6	0.5	3	3	3
Eu	0.1	0.1	0.1	0.4	0.1	0.2	0.2	0.2
Gd	1.5	2.2	4.3	6.3	0.5	3	3	3
Tb	0.5	1	1.3	1.3	0.1	1	1	1
Dy	3.5	10	10	8.5	2	7	8	7
Ho	1	3	2	2	0.5	2	2	2
Er	3.5	10	7	6	2	6.8	6.7	6
Tm	0.6	2	1.2	1	0.3	1.2	1.3	1
Yb	4	15	9	6	2	8	8.85	8
Lu	0.6	2.2	1.2	1	0.4	1.2	1.3	1
∑LREE	10.9	20.7	79.7	106.9	20.2	39.9	36.5	45
CC1	0.07	0.13	0.50	0.67	0.13	0.25	0.23	0.3
∑HREE	15.2	45.4	36	32.1	7.8	30.2	32.15	28
CC2	0.48	1.45	1.15	1.02	0.25	0.96	1.02	1
∑REE	26.1	66.1	115.7	139	28	70.1	68.65	73
CC3	0.14	0.35	0.61	0.73	0.15	0.37	0.36	0.4
Ce*	1.16	1.07	1.35	1.09	0.7	1.4	1.2	1.1
Eu*	0.25	0.25	0.08	0.77	0.26	0.26	0.26	0.2
t1	1.20	1.10	1.31	1.08	0.47	1.32	1.18	1.09
t3	1.26	1.43	1.43	1.09	1.04	1.26	1.35	1.27
t1-3	**1.25**	**1.28**	**1.4**	**1.1**	**0.7**	**1.32**	**1.3**	1.2
t4	1.08	1.09	1.10	0.98	0.82	1.05	1.10	1.03
t1-4	**1.14**	**1.09**	**1.20**	**1.03**	**0.62**	**1.18**	**1.14**	1.06
Y/Ho	196	52	103	91	368	88	91	141
Sr/Eu	280	360	260	130	100	180	175	212
REEs/HREEs	0.7	0.5	2.2	3.3	2.6	1.3	1.1	2

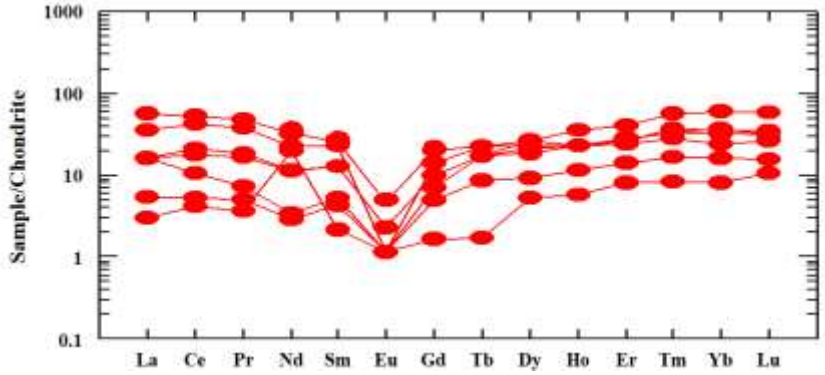

Fig. 24 Normalized REE patterns of the studied psammitic gneiss. The chondritic values are from [56].

6.3 Tetrad phenomena

Visual inspection suggests that the third tetrad in most samples is more prominent than the first and fourth curved segments. The second tetrad is comparably difficult to recognize due to the anomalous behavior of Eu and the fact that Pm does not occur in nature. Figure (24) and Table (2) show that the studied gneisses have strong M-type tetrad effect in the third tetrad. On the contrary, these rocks have lower values in the fourth tetrad with respect to the third segment and show strong W-type tetrad effect in sample B5. The presence of complex M-W type tetrad phenomena, suggest changes in physico-chemical conditions that prevailed during hydrothermal alteration of these rocks and may illustrate the presence of gold mineralization as confirmed by mineralogical studies. MW-type tetrad effect may result from the interaction of aqueous liquids with alkaline rocks **[57]**.

6.4 Fractionation of isovalents

6.4.1 Nb/Ta and Zr/Hf ratios

Nb and Ta have the same charge and ionic radius, so, their behavior in the geochemical processes are similar [58]. Though, their identical behavior, recorded Nb/Ta ratios are variable in different igneous systems like granites, peraluminous granites, and late magmatic fluids [59], [60], [61], [58], [62], suggesting their fractionation. The mobilization of Nb increases with temperature. [60]. This means that high Nb/Ta ratios occur in high-temperature deposits, which may be connected to the destruction of biotite that contains Nb contents. In spite of their fractionations (Nb and Ta) increase with fluid temperatures [63], their solubilities in F-bearing solutions increase under reducing low temperatures conditions [64]. According to [65], the chondritic value of Nb/Ta is 17.6 ± 1, Most samples have subchondritic Nb/Ta values while two samples only have suprerchondritic values (Table 1). The subchondritic values could be related to the M-type tetrad effect inherited from the surrounding granitic rocks while the suprerchondritic values connected to the solubility of these elements in low temperature F-bearing solutions. [66] reported Zr/Hf and Nb/Ta values range in oceans and sea waters are high (45-350 and 14-85, respectively). This may show that the low temperature F-rich solutions could be sea or oceanic water. Zr, Hf, Nb, and Ta are highly soluble in the sea waters and oceans, so, Zr/Hf and Nb/Ta ratio could be an indication parameter to clarify the paleo-conditions of marine environments [67]. Zr/Hf Chondritic values are within the range of 26–46 [68]. All the studied gneisses have superchondritic Zr/Hf ratio values, suggesting that the fractionation of Zr, Hf, Nb and Ta could be related to the effect of sea or oceanic water (Table 1). The subchondritic and suprerchondritic values could be related to M- and W-type tetrad effects.

6.4.2 Y/Ho ratios

Geochemically trivalent pairs such as Y and Ho represent similar behavior during geochemical processes in various geological environments such as seawater column and magmatic/hydrothermal systems [69], [70]. Moreover, fraction between these isovalent pairs due to different surface complex stabilities and rapid scavenging of Ho by Fe- and/or Mn- (hydro-) oxides lead seawaters to have Y/Ho ratios of 50-60 [71], [72], [73]. The gneisses have Y/Ho ratio ranges between 52 and 368, suggesting the effect of sea and ocean water in scavenging Ho with respect to Y.

6.4.3 Sr/Eu ratio

Sr/Eu ratio chonderitic value is 220 [74]. Sr/Eu ratio average of the studied gneisses is 212.13, which is lesser than the chonderitic value, which may related to the later alteration processes.

7 Radioactivity

Distribution of radioelements in the studied rocks

Radiometric measurements using NaI (Tl) detector for radionuclides indicate that eU, eTh, RaeU and potassium ranges are (7.2-78 ppm), (11-62 ppm), (6-121 ppm) and (0.7-5.6 wt.%), with averages 25.8, 27.75, 30.17 and 3.57, respectively. The studied gneisses are considered high uranium high thorium rocks. Comparing the studied gniesses with similar local and international averages of radionuclides illustrate that these rocks have higher averages (Table 3). The high contents of the radioelements are mainly connected to the presence of radioactive minerals and radioelement-bearing minerals as clarified in the mineralogical studies.

7.1 Equilibrium and disequilibrium

The equilibrium state of the studied samples can be determined by calculating the equilibrium factor (P) which is the ratio of the radiometric uranium (eU) to the radium content (Ra) i.e., P-factor = eU/RaeU. If the P-factor is greater than unity it means that recent addition of uranium took place, while P-factor <1 indicates recent removal of uranium. According to the above statements the gneisses samples in disequilibrium state P factor, where most samples have values lesser than unity, while the others are higher. the divergence of the samples may show the changes in the physic-chemical conditions that lead to complex process of removal and addition of uranium [79], [80].

7.2 D-factor

D-factor is the ratio between the chemically determined uranium and the radiometrically-measured uranium [81]. If the D-factor was more or less than unity, it indicates addition or removal of uranium respectively [81] and [82]. Results of confirm D-factor confirm the

removal addition process of P-factor, suggesting vigorous changes in physic-chemical conditions (Table 3).

7.3 Authigenic uranium

The ratio of U_{ch}/Th_{ch} may be used as a redox indicator; U/Th ratio below 1.25 suggests oxic conditions whereas values above 1.25 suggest suboxic and anoxic conditions **[83]).** The U_{ch}/Th_{ch} ratio (Av. 0.5 -0.93) in psammitic gneiss and spot anomaly respectively; indicates oxic condition.

The authigenic uranium content is calculated as (Authigenic U) = U-Th/3. Values of authigenic uranium below 5 are thought to represent oxic condition, while values above 5 are indicative of suboxic to anoxic condition. The paragneiss samples value (Av.4.1) indicates oxic condition.

7.4 Uranium mobilization

The equation eU-(eTh/3.5) reflects the uranium mobilization. If result of this equation equals zero, it indicates that no uranium mobilization took place (i.e. fresh samples). When it is greater than zero it means that uranium was enriched (added to rock). The negative values mean uranium leaching out.

Nearly all samples of Skait gneisses plot above zero line, it means that uranium enrichments took place (Fig.25).

7.5 Type and amount of mobilization

The type (migration in or migration out) and amount of the mobilized uranium as well as its mobilization rate are calculated through the equations of **[84]**.

(a) To calculate paleo-uranium background (i.e., original uranium content U), which means to multiply the average Th content detected from γ-ray spectrometric survey by average regional U/Th ratio.

$$\mathbf{U_0 = eTh^* \; eU/eTh} \qquad (1)$$

Where eTh* = is the average of the thorium content in a given geological unit; eU /eTh= the average regional eU/eTh ratio.

(b) To calculate the amount of mobilized uranium (i.e., the amount of uranium migration U_m) through the following equation:

$$\mathbf{U_m = U_p - U_0} \qquad (2)$$

Where U_p means the average uranium content.

If $U_m > 0$, uranium migrated in the geologic body during late evolution.

If $U_m < 0$, uranium lost in the geologic body during late evolution.

If $U_m > 2$, lots of uranium migrated in.

If $U_m < -2$, lots of uranium migrated out.

$-2 < U_m < 2$, migration equivalent in and out.

(c) To calculate the mobilized uranium migration rate.

$$P\% = U_m/U_p \times 100 \qquad (3)$$

The values in the studied Skait gniesses are

U0=1.11x26 = 28.81 Um= 22.22-28.81= -6.59

P=(-6.59/22.22)x 100= -29.66

According to the above statements the U_m value of gneiss samples indicate lots of uranium migrated out, which confirm equilibrium-disequilibrium studies.

8 Summary and Conclusion

The area lies between latitudes 24°38′ 36″to 24° 39’ 21″N and longitudes 34° 47′ 03″ to 34° 48′ 06″E composed mainly of tectono-stratigraphic sequence begins from the oldest as psammitic gneiss, ophiolitic mélange, monzogranites, and lamprophyre dykes. The gneisses striking NNE-SSW. gneisses are jointed, sheared, mylonitized, and hematized. Petrographical study cleared that the psammitic gneiss composed of quartz, plagioclase, biotite in addition to a less frequent amount of potash feldspar (microcline, microcline-perthite). Zircon, monazite, sericite, cordierite, and opaques are common accessory phases. Radioactive material was recorded as yellow amorphous material associated with iron oxides filling the late-stage fractures associating with iron oxides. Mineralogical studies show the presence of radioactive minerals (kasolite, torbernite, thorite, and uranothorite), base metals (gold, bismite, cassiterite, chalcocite, and Sphalerite), Nb-Ta minerals (aeschynite and columbite), and accessory minerals (zircon and xenotime). Geochimcal investigation indicated that origin of Sikait psammitic gneiss were sedimentary origin. Radiometric investigations exhibit that the gneisses are high uranium high thorium rocks and the evidences of uranium migration. Rare earth patterns of these rocks indicate that these rocks are subjected to hydrothermal alterations and affected by water rich solutions, which are confirmed complex M-W tetrad effects and fractionation of isovalents. M-W tetrad effects clarify vigorous physic-chemical changes and the presence of uranium mineraliation.

Acknowledgement

The author sincerely thanks the late Prof. Mohamed E. Ibrahim for suggesting the research point. Also thankfully acknowledge Prof. Gehad Saleh, vice president of Nuclear Materials Authority, Prof. Mohamed Galal. El Feky, prof. Mohamed Salem Kamr, and Assistant. Prof. Amira El-Tohami for supporting this work.

Table 3 Spectrometric measurements and chemical analysis of psammitic gneiss, Wadi Sikait, SED, Egypt

No	eU	eTh	RaeU	K %	U_{ch} (ppm)	Th_{ch} (ppm)	U_{ch} / Th_{ch}	P -factor eU/RaeU	D-factor U_{ch}/eU	authigenic U	eU/ eTh
1	78	17	121	0.7	15	20	0.8	0.64	0.19	8.3	4.59
2	11	11	23	3.4	13	25	0.5	0.48	1.18	4.7	1.00
3	17	18	13	2.9	16	8	2.0	1.31	0.94	13.3	0.94
4	7.2	23	9	2.3	7	8	0.9	0.80	0.97	4.3	0.31
5	19	62	6	4.8	13	31	0.4	3.17	0.68	2.7	0.31
6	13	31	19	5	7.5	30	0.3	0.68	0.58	-2.5	0.42
7	11	28	15	5	7	24	0.3	0.73	0.64	-1.0	0.39
8	8.5	18	13	3.7	20	40	0.5	0.65	2.35	6.7	0.47
9	16	33	9	5.6	8.8	20	0.4	1.78	0.55	2.1	0.48
10	41	19	7	3.1	8.7	20	0.4	5.86	0.21	2.0	2.16
Min.	7.2	11	6	0.7	7	8	0.3	0.48	0.19	-2.5	0.31
Max.	78	62	121	5.6	20	40	2	5.86	2.35	13.3	4.59
Av.	25.58	27.75	30.17	3.57	11.92	22.83	0.73	1.87	0.90	4.28	1.33
Metamorphosed sandstone [75]	12.00	19.00	10.64	3.18	-	-	-	-	-	-	-
Arenaceous sediments [76] and [77]	1	3	-	1.4	-	-	-	-	-	-	-
Argillaceous sediments [76] and [77]	4	16	-	2.7	-	-	-	-	-	-	-
Average of greywacke [78]	1.5	5	-	-	-	-	-	-	-	-	-

- Not determined

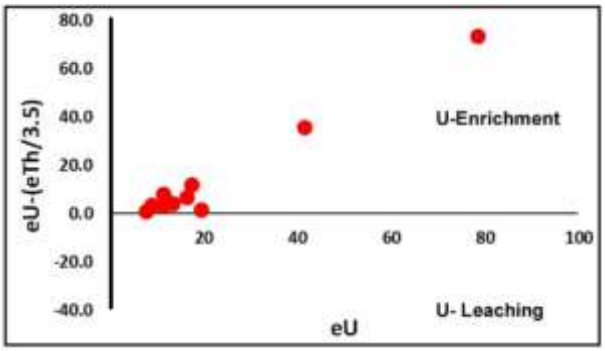

Fig. 25 Uranium mobilization in Wadi Sikait psammitic gneiss.

References

[1] R.O. Greiling, A. Kröner, M.F. El Ramly, and A.A. Rashwan, Structural relationships between the southern and central parts of the Eastern Desert of Egypt: details of a fold and thrust belt. In: El Gaby, S., Greiling, R.O. (Eds.). The Pan-African Belt of Northeast Africa and Adjacent Areas. Vieweg and Sohn, Weisbaden, 121– 145, 1988**.**

[2] H Fritz, E. Wallbrecher, A.A. Khudier, F. Abu El Ela, and R.D. Dallmeyer, Formation of Neoproterozoic metamorphic core complexes during oblique convergence, Eastern Desert, Egypt. J Afr Earth Sci 23, 311–329, 1996.

[3] AE Abdel Gawad, MM Ghoneim, A. El-Taher, AA Ramadan ., Mineral chemistry aspects of U-, Th-, REE-, Cu-bearing minerals at El-Regeita shear zone, South Central Sinai, Egypt. Arabian Journal of Geosciences 14, 1-13, 2021.

[4] M.E Ibrahim, and A.A. Ragab, Geochemistry of lamprophyre dykes, Wadi Sikait area, South Eastern Desert, Egypt. Chin. J. Geochem. 30, 323–331, 2011**.** https://doi.org/10.1007/s11631-011-0516-4.

[5] G.M Saleh, S.A Abdallah, A. A. Abbas, N.A. Dawood, and M.A.Rashed,. Uranium mineralizations of Wadi Sikait mylonites, Southeastern Desert, Egypt. Jor. of Geo. and Min. Res. 3(5), 86-104, **2012**. https://doi.org/10.5897/JGMR10.035

[6] I.H. Ibrahim, Abu Rusheid-Sikait Mylonitic Rocks, South Eastern Desert, Egypt: Origin and Mode of Occurrence. Inter. Conf. on Nat. Haz. and Geomatics -ICNHG, Tunisia, **2013.**

[7] AE Abdel Gawad, MA Ali, MM Ghoneim, A. El-Taher., Natural radioactivity and mineral chemistry aspects of rare metal mineralization associated with mylonite at Wadi Sikait, South Eastern Desert, Egypt. International Journal of Environmental Analytical Chemistry, 1-18. 2021.

[8] M.S Kamar, A.M. El-Tohamy, H.I. Mira, and A.M. Ismail, Geology and Environmental Impact Assessment of Psammitic Gneiss and Lamprophyre Dykes at Wadi Sikait, South Eastern Desert, Egypt. J. Phys.: Conf. Ser. 2305 012001, 2022. doi:10.1088/1742-6596/2305/1/012001

[9] H.S. Assaf, M.E. Ibrahim, A.A. Zalata, A.A. El-Metwally, and G.M. Saleh Polyphase folding in Nugrus-Sikait area south Eastern Desert Egypt. JKAW: Ear. Sci., 12, 1-16., 2000.

[10] P.R. Johnson, A.Andresen, A.S. Collins, A.R. Fowler, H. Fritz, W. Ghebreab, T. Kusky, and R.J. Stern, Late Cryogenian–Ediacaran history of the Arabian–Nubian Shield: A review of depositional, plutonic, structural, and tectonic events in the closing stages of the northern East African Orogen. Jour. of Afr. Ear. Sci., 61, 167–232, 2011**.**

[11] L.i. Tung, and Y. Chi-Lung, The abundance of chemical elements in the earth's crust and its major tectonic units: Scientia Sinica, 15, no. 2, 258-272, 1966.

[12] A.M. Evans, Ore Geology and Industrial Minerals, An Introduction, Blackwell,.403, 1993.

[13] C.G Durieux, and A.C. Brown. Geological context, mineralization, and timing of the Juramento sedimenthosted stratiform copper–silver deposit", Salta district northwestern Argentina. Miner. Deposita, 42, 879– 899, 2007

[14] J Guilbert, and C. Park, The Geology of Ore Deposits: W.H. Freeman and Co., New York, 985 pp, 1986

[15] A. A. Surour, A. A. El-Kammar, E. H. Arafa, and H. M. Korany, Dahab stream sediments, South Eastern Sinai, Egypt: a potential source of gold, magnetite and zircon. Jour. of Geoch. Expl., 77, 25-43, 2003

[16] A.M. Dardier, Morphology and geochemistry of zircon associated with uranium mineralaization in Gattar granitic pluton, North Eastern Desert, Egypt. Egyptian J. Geol., 42(1): 75-103, 1999.

[17] A.M. Abdel Warith, M.F. Raslan, and M.A. Ali, Mineralogy and Radioactivity of Pegmatite Bodies from the Granitic Pluton of Gabal Um Taghir El-Tahatani Area, Central Eastern Desert, Egypt [C]. The 10th Int. Min. Petrol & Metallurg. Eng. Conf. Mining. 24–41, 2007.

[18] M.R. Bhatia, and K.A.W. Crook, Trace element characteristics of greywacke and tectonic setting discrimination of sedimentary basins: Contr. to Min. and Petr.,. 92, 181–193.,1986.

[19] B.P. Roser, and R. J. Korsch, Determination of tectonic setting of sandstone-mudstone suites using SiO_2 content and K_2O/Na_2O ratio. Jour. of Geo. 94, 635-650, 1986.

[20] J. E Otamendi, and A. E. Patiño Douce, Partial melting of aluminous metagreywackes in the Northern Sierra de Comechingones, Central Argentina. Journal of Petrology, 42, 1751–1772, 2001.
http://dx.doi.org/10.1093/petrology/42.9.1751.

[21] C. Augustsson, and H. Bahlburg, Active or passive continental margin? Geochemical and Nd isotope constraints of metasediments in the backstop of a pre-Andean accretionary wedge in southernmost Chile (46°30'–48°30'S). In: Tracing Tectonic Deformation Using the Sedimentary Record (McCann, T. & Saintot, A.; Eds.), Geo. Soc., London, Special Publications, 208, 253–268, 2003. http://dx.doi.org/10.1144/GSL.SP.2003.208.01.12.

[22] M.M. Abu El-Enen, Geochemistry and metamorphism of the Pan-African back-arc Malhaq volcano-sedimentary Neoproterozoic association, W. Kid area, SE Sinai, Egypt. Jour. of Afri. Ear. Sci., 51, 189–206, 2008.
http://dx.doi.org/10.1016/j.jafrearsci.2008.01.004.

[23] M.M. Abu El-Enen, Geochemistry, provenance, and metamorphic evolution of Gabal Samra Neo-proterozoic metapelites, Sinai, Egypt. Jour. of Afr. Ear. Sci., 59, 269–282. 2011. http://dx.doi.org/10.1016/j.jafrearsci.2010.11.002.

[24] C.D. Werner, Saxonian granulites: a contribution to the geochemical diagnosis of original rocks in high-metamorphic complexes. Gerlands Beitraegezur Geophysik, 96: 271–290, 1987.

[25] D. Garcia, J. Coelho, and M. Perrin, Fractionation between TiO2 and Zr as a measure of sorting within shale and sandstone series (northern Portugal). Eur. Jour. of Miner., 3: 401–414,1991. http://dx.doi.org/10.1127/ejm/3/2/0401.

[26] M. M. Herron, Geochemical classification of ter-rigenous sands and shales from core or log data. Jour. of Sed. Petr., 58, 820–829, 1988. http://dx.doi.org/10.1306/212F8E77-2B24-11D7-8648000102C1865D.

[27] R. M. Garrels, and E. T. Mackenzie,. Evolution of sedimentry rocks: New York, W.W. Norton, 227p, 1971

[28] S. M. McLennan, Weathering and Global Denudation. Journal of Geology, 101, 295–303, 1993.

[29] R. Cox, D.R. Lowe, and R.L. Cullers, The Influence of Sediment Recycling and Basement Composition on Evolution of Mudrock Chemistry in the Southwestern United-States. Geo. et Cosm. Acta, 59, 2919–2940, 1995.

[30] H. W. Nesbitt, and G. M. Young, Early Proterozoic climates and plate motions inferred from major element chemistry of lutites. Nature, 299, 715–717, 1982. http://dx.doi.org/10.1038/299715a0.

[31] C. M. Fedo, H. W. Nesbitt, & G. M. Young, Unraveling the effects of potassium metasomatism in sedimentary rocks and paleosols, with implications for paleoweathering conditions and provenance. Geology, 23, 921-924, 1995. http://dx.doi.org/10.1130/0091-7613(1995)023<0921:UTEOPM>2.3.CO;2.

[32] J.A. Winchester, and M. D. Max, The geochemistry and origin of the Precambrian rocks of the Rosslare Complex, SE Ireland. Jour. of the Geo. Soci, London 139, 309–319, 1982.

[33] R.M. Garrels, F.T. Mackenzie, Evolution of Sedimentary Rocks. Norton, NewYork, p. 397, 1971.

[34] C. Meyer, J.J. Hemley, Wall rock alteration in geochemistry of ore deposits, H. L. Barnes, ed., New York: pp 166-235, 1967.

[35] H. Paulick, W. Herrmann, J.B. Gemmel, Alteration of felsic volcanics hosting the Thalanga massive sulfide deposit (Northern Queensland, Australia) and geochemical proximity indicators to ore. Economic Geology 96, 1175-1200, 2001.

[36] H.W. Nesbitt, and G.M. Young, Early Proterozoic Climates and Plate Motions Inferred from Major Element Chemistry of Lutites. Nature, 299, 715-717, 1982.

[37] C.M. Fedo, Grant, G.M., and Nesbitt, H.W., 1997. Paleoclimatic control on the composition of the Paleoproterozoic Serpent Formation, Huronian Supergroup, Canada: a greenhouse to icehouse transition. Precamb. Res., 86, 201–223.

[38] H. W. Nesbitt, and G. M. Young, Prediction of some weathering trends of plutonic and volcanic rocks. based on thermodynamic and kinetic considerations. Geoch. et Cosm. Acta, 48, 1523–1534, 1984. http://dx.doi.org/10.1016/0016-7037(84)90408-3.

[39] H. W. Nesbitt, and G. M. Young, Formation and diagenesis of weathering profiles. Jour. of Geo. 97, 129–147, 1989. http://dx.doi.org/10.1086/629290.

[40] H. W. Nesbitt, G. M. Young, S. M. McLennan, and R. R. Keays, Effects of chemical weathering and sorting on petrogenesis of siliciclastic sediments, with implications for provenance studies. Jour. Geol., 104, 525-542. 1997 .http://dx.doi.org/10.1086/629850.

[41] S.R. Taylor, and S.M. McLennan, The Continental Crust: Its Composition and Evolution. Blackwell, Oxford. 1985.

[42] L. Harnois, The C. I. W. index: a new chemical index of weathering. Sed. Geo., 55, 319–322. 1988. http://dx.doi.org/10.1016/0037-0738(88)90137-6.

[43] S. M. McLennan, S. R. Taylor, and K. A. Eriksson, Geochemistry of Archeanshales from the Pilbara Supergroup, Western Australia. Geochim. Cosm. Acta, 47, 1211–1222. 1983. http://dx.doi.org/10.1016/0016-7037(83)90063-7.

[44] G. Mongelli, R.L. Cullers, and S. Muelheisen, Geochemistry of Late Cretaceous-Oligocenic shales from the Varicolori Formation, southern Apennines, Italy: implications for mineralogical, grain-size control and provenance, Eur. J. Mineral., 8, 733–754. 1996.

[45] G. Voicu, M. Bardoux, L. Harnois, and R. Grepeau, Lithological and geochemical environment of igneous and sedimentary rocks at Omai gold mine, Guyana, South America. Expl. and Min. Geo. 6, 153-170, 1997.

[46] L.J. Suttner, and P.K. Dutta, Alluvial sandstone composition and palaeoclimate, I. Framework mineralogy. Jour. of Sed. Petr. 56(3), 329-345. 1986.

[47] R. R. Large, J. B. Gemmell, H. Paulik The alteration box plot: A simple approach to understanding the relation between alteration mineralogy and lithogeochemistry associated with volcanic-hosted massive sulfide deposits. Econ. Geology. 96: 957-971. 2001.

[48] T.H. Green, A.O. Brunfeld, & K.S. Heyer, Rare earth element distribution and K/Rb ratios in granulites, mangerites and anorthosites, Lofoten-Vesteraalen, Norway. Geoch. et Cosm. Acta 36,

241-257, 1972.

[49] A. El-Taher, WM Badawy, AEM Khater, HA Madkour., Distribution patterns of natural radionuclides and rare earth elements in marine sediments from the Red Sea, Egypt. Applied Radiation and Isotopes 151, 171-181.

[50] Wronkiewicz, D. J., and Condie, K. C., 1987. Geochemistry of Archean shales from the Witwatersrand Supergroup, South Africa: source-area weathering and provenance. Geochim. Cosm.. Acta, 51, 2401–2416. http://dx.doi.org/10.1016/0016-7037(87)90293-6

[51] Cullers, R.L. 1994. The controls on the major and trace element variation of shales, siltstones and sandstones of Pennsylvanian – Permian age from uplifted continental blocks in Colorado to platform sediment in Kansas, USA, Geoch. et Cosmoch.Acta, 58(22), 4955-4972.

[52] R.L. Cullers, and J. Graf, Rare earth element in igneous rocks of the continental crust: intermediate and silicic rocks, ore petrogenesis In Henderson, P. (ed.), Rare ear. Geoch., Elsev, 275-316, 1984.

[53] A. K. Singh, R. K. B. Singh, and G. Vallinayagan, Anorogenic acid volcanic rocks in the Kundal area of the Malani igneous suite, Northwestern India: geochemical and petrogenetic studies. Jour. of Asian Ear. Sci., 1-14, 2006.

[54] T. Grenne, and D. Roberts, The Holondaporphyrite , Norwegian Caledonides: geochemistry and tectonic setting of Early- Mid. Ordovician shoshonite volcanism . J. Geol. Soc.,London, Vol. 155, 131-142, 1998.

[55] L. N. Ovchinnikov, Applied geochemistry (in Russian). Nedra, Moscow, 1990.

[56] S. S. Sun, Lead isotopic study of young volcanic rocks from mid-ocean ridges, oceanic islands and island arcs. Philophical Transactions of the Royal Society of London, vol. A 297, p. 409-445, 1980.

[57] Z.H. Zhao, Z.W. Bao, G.U Lee Seung, A composite M- with W-type of REE tetrad effect in a north China alkaline complex. Geochim Cosmochim Acta 72 Supp:11095, 2008

[58] C. Ballouard, M. Poujol, P. Boulvais, Y. Branquet, R. Tartèse, & J.l. vigneresse, Nb-Ta fractionation in peraluminous granites: A marker of the magmatic-hydrothermal transition. – Geology, 44: 231-234, 2016

[59] R. Tartese, & P. Boulvais, Differentiation of peraluminous leucogranites “en route” to the surface. – Lithos, 114: 353-368, 2010

[60] A. Stepanov, J.A Mavrogenes, S. Meffre, & P. David Son, The key role of mica during igneous concentration of tantalum. – Contributions to Mineralogy and Petrology, 167: 1009-1016, 2014

[61] J. Dostal, D. J. Kontak, O. Gerel, J.G. Shellnutt, & M. Fayek, Cretaceous ongonites (topaz-bearing albite-rich microleucogranites) from Ongon Khairkhan, Central Mongolia: Products of extreme magmatic fractionation and pervasive metasomatic fluid: rock interaction. – Lithos, 236-237: 173-189, 2015

[62] A. Abedini, M. R. Azizi, and A. A. Calagar, The Lanthanide Tetrad Effect in Argillic Alteration: An Example from the Jizvan District, Northern Iran. Acta Geologica Sinica,, 92, 4 , 1468–1485, 2018

[63] E.V. Badanina, L.F. Syritso, E.V. Volkova, R. Thomas, R.B. Trumbull, Composition of Li-F granite melt and its evolution during the formation of the orebearing Orlovka massif in Eastern Transbaikalia. Petrology 18, 131–157, 2010

[64] G.P. Zaraisky, V. Korzhinskaya, N. Kotova, Experimental studies of Ta2O5 and columbite-tantalite solubility in fluoride solutions from 300 to 550 °C and 50 to 100 MPa. Mineral. Petrol. 99, 287–300, 2010.

[65] B.M. Jahn, F Wu, R. Capdevila, F. Martineau, Z. Zhao, Y. Wang, Highly evolved juvenile granites with tetrad REE patterns: the Woduhe and Baerzhe granites from the Great Xing'an Mountains in NE China. Lithos 59, 171–19. 2001.

[66] M. L. Firdaus, T. Minami, K. Norisuye, & Y. Sohrin, Strong elemental fractionation of Zr-Hf and Nb-Ta across the Pacific Ocean. – Nature Geosciences, 4: 227-230, 2011

[67] K. Schmidt, M. Bau, J. hein, & a. koschinsky, Fractionation of the geochemical twins Zr-Hf and Nb- Ta during scavenging from seawater by hydrogenetic ferromanganese crusts. – Geochimica et Cosmochimica Acta, 140: 468-487. 2014

[68] M. Bau, A. Koschinsky, P. Dulski, and J.R. Hein, Comparison of the partitioning behaviours of yttrium, rare earth elements, and titanium between hydrogenetic marine ferromanganese crusts and seawater. Geochimica et Cosmochimica Acta, 60: 1709–1725, 1996.

[69] R.D. Shannon, Revised effective ionic radii and systematic studies of interatomic distances in halides and chalcogenides. Acta Crystallographica B, 25: 925–946, 1976.

[70] M.G. Gadd, D. Layton-Matthews, & J.M. Peter, Non-hydrothermal origin of apatite in SEDEX mineralization and host rocks of the Howard’s Pass district, Yukon, Canada. – American Mineralogist, 101: 1061-1071, 2016

[71] M. Minami, A. Masuda, K. Takahashi, M. Adachi, & H. Shimizu, Y-Ho fractionation and lanthanide tetrad effect observed in cherts. –

Geochemical Journal, 32: 405-419, 1998

[73] Z. Maksimovic, G.Y. Pantó, Contribution to the geochemistry of the rare earth elements in the karst-bauxite deposits of Yugoslavia and Greece. Geoderma 51, 93‑109. 1991.

[74] Neveen S. Abed , Mohamed G. El Feky, Atef El-Taher, Ehab El Sayed Massoud, Mahmoud R. Khattab, Mohammed S. Alqahtani, El Sayed Yousef and Mohamed Y. Hanfi, Geochemical Conditions and Factors Controlling the Distribution of Major, Trace, and Rare Elements in Sul Hamed Granitic Rocks, Southeastern Desert, Egypt., Minerals 2022, 12, 1245, 2022.

[75] S. A. Abu Elatta, S. F. Hassan, A. H. El-Farrash, M. G. El-Feky, and M. Refaat, Recent Uranium Mobilization and Radioactivity of Metamorphosed Sandstones at Sikait Area, Southeastern Desert, Egypt., Journal of Geology and Mining Research, 6 (2), 28-38, 2014

[76] IAEA, International Atomic Energy Agency. "Gamma-Ray Survey in Uranium Exploration". IAEA Technical Report Series, No. 186, Vienna, Austria, pp. 90.,1979

[77] R. W. Boyle, Geochemical prospecting for thorium and uranium deposits. Elsevier Publ. Co., Amsterdam, 498 p, 1982

[78] P.G. Killeen, Gamma ray spectrometric methods in uranium exploration—application and interpretation; in Geophysics and Geochemistry in the Search for Metallic Ores; Hood, P.J., ed., Geol. Surv. Can., Economic Geology Report 31, p. 163-229, 1979

[79] S A. Taalab, W H. Mohamed, S A. Shetaia, M. Al Meshari, Y. Alzamil, A. Abanomy, A. Alyahyawi, A. El-Taher., Radiological and environmental hazards of granitic rocks in Wadi Faliq El Sahl and El Waar area, North Eastern Desert, Egypt. Journal of Environmental Science and Health, Part A, 1-16. 2023.

[80] HA Awad, HMH Zakaly, AV Nastavkin, AM El Tohamy, A. El-Taher., Radioactive mineralization's on granitic rocks and silica veins on shear zone of El-Missikat area, Central Eastern Desert, Egypt. Applied Radiation and Isotopes 168, 109493. 2021.

[81] J.D. Hansink, Equilibrium analyses of sandstone roll-front uranium deposits, International Atomic Energy Agency, Vienna, 683-693. 1976.

[82] J.S. Stuckless, I.T. Nkomo, D.B. Wenner, and G. Van Trump, Geochemistry and uranium favourability of the post-orogenic granites of the northwestern Arabian Shield, Kingdom of Saudi Arabia. In: Pan African crustal evolution in the Arabian –Nubian Shield (Convenor, A.M. Alshanti), Bull. Fac. Earth Sci. KAU (Jeddah), 6, 195-210, B. Bergamon Press. Oxford., 1984

[83] B.N. Nath, M. B.R. Bau, , C.M. Rao, Trace, and rare earth elemental variationnin Arabian Sea sediments through a transect across the oxygen minimum zone. Geochim. Cosmochim. Acta 61, 2375–2388, 1997.

[84] Benzing Uranium Institute, Field Gamma-ray Spectrometric Survey, No.3, , 1:292, China. 1977